

# The Landfall and Inland Penetration of a Flood-Producing Atmospheric River in Arizona. Part I: Observed Synoptic-Scale, Orographic, and Hydrometeorological Characteristics

PAUL J. NEIMAN AND F. MARTIN RALPH

*Physical Sciences Division, NOAA/Earth System Research Laboratory, Boulder, Colorado*

BENJAMIN J. MOORE, MIMI HUGHES, AND KELLY M. MAHONEY

*Cooperative Institute for Research in the Environmental Sciences, NOAA/ESRL, Boulder, Colorado*

JASON M. CORDEIRA

*National Research Council, NOAA/ESRL, Boulder, Colorado*

MICHAEL D. DETTINGER

*U.S. Geological Survey, and Scripps Institution of Oceanography, La Jolla, California*

(Manuscript received 11 July 2012, in final form 6 September 2012)

## ABSTRACT

Atmospheric rivers (ARs) are a dominant mechanism for generating intense wintertime precipitation along the U.S. West Coast. While studies over the past 10 years have explored the impact of ARs in, and west of, California's Sierra Nevada and the Pacific Northwest's Cascade Mountains, their influence on the weather across the intermountain west remains an open question. This study utilizes gridded atmospheric datasets, satellite imagery, rawinsonde soundings, a 449-MHz wind profiler and global positioning system (GPS) receiver, and operational hydrometeorological observing networks to explore the dynamics and inland impacts of a landfalling, flood-producing AR across Arizona in January 2010. Plan-view, cross-section, and back-trajectory analyses quantify the synoptic and mesoscale forcing that led to widespread precipitation across the state. The analyses show that a strong AR formed in the lower midlatitudes over the northeastern Pacific Ocean via frontogenetic processes and sea surface latent-heat fluxes but without tapping into the adjacent tropical water vapor reservoir to the south. The wind profiler, GPS, and rawinsonde observations document strong orographic forcing in a moist neutral environment within the AR that led to extreme, orographically enhanced precipitation. The AR was oriented nearly orthogonal to the Mogollon Rim, a major escarpment crossing much of central Arizona, and was positioned between the high mountain ranges of northern Mexico. High melting levels during the heaviest precipitation contributed to region-wide flooding, while the high-altitude snowpack increased substantially. The characteristics of the AR that impacted Arizona in January 2010, and the resulting heavy orographic precipitation, are comparable to those of landfalling ARs and their impacts along the west coasts of midlatitude continents.

## 1. Introduction

Atmospheric rivers (ARs) are long (>2000 km), narrow (<1000 km), low-level (below ~600 hPa) plumes of enhanced water vapor flux (e.g., Zhu and Newell 1998;

Ralph et al. 2004, 2005, 2011; Neiman et al. 2008a,b; Smith et al. 2010) embedded within a broader region of generally poleward heat transport in the warm sector of maritime extratropical cyclones commonly referred to as the "warm conveyor belt" (e.g., Browning 1990; Carlson 1991). During the last few years, research focused along the west coasts of continents demonstrated cool-season linkages between ARs and heavy precipitation (e.g., Dettinger 2004; Ralph et al. 2011; Stohl et al. 2008; Reeves et al. 2008; Neiman et al. 2008a,b, 2009,

---

*Corresponding author address:* Paul J. Neiman, Physical Sciences Division, NOAA/Earth System Research Laboratory, Mail Code R/PSD2, 325 Broadway, Boulder, CO 80305.  
E-mail: paul.j.neiman@noaa.gov

2011; Smith et al. 2010; Viale and Nuñez 2011; Dettinger et al. 2011; Ralph and Dettinger 2012), ARs and snowpack variability (e.g., Neiman et al. 2008b; Guan et al. 2012), and ARs and floods (e.g., Dettinger 2004; Ralph et al. 2003, 2006, 2011; Dettinger et al. 2011; Lavers et al. 2011; Neiman et al. 2011). In addition to causing severe weather with adverse societal impacts across the semiarid West Coast states, ARs also contribute significantly to long-term water resources there (e.g., Dettinger et al. 2011).

Many studies have focused on orographically enhanced hydrometeorological impacts of ARs west of the Sierra Nevada and Cascade Mountains, but their influence downwind across the intermountain west of the United States remains an open question. For example, how much water vapor transport occurs through gaps in the mountains, and how much vapor remains in the atmosphere after passing over higher topography? The synoptic and mesoscale meteorology may also come into play in order for heavy precipitation to occur in the interior, such as the direction of the flow relative to steep mountain barriers, the ambient static stability, and the intensity of transient disturbances. A parallel track of research in recent years has explored the modification of fronts and cyclones as they migrate across the complex topography of the intermountain west (e.g., Steenburgh and Blazek 2001; Shafer et al. 2006; Steenburgh et al. 2009; West and Steenburgh 2010, 2011). However, those studies do not address the evolution of ARs, or their hydrometeorological impacts, if any, as they penetrated inland from the Pacific. A study by Leung and Qian (2009) has taken a useful step toward filling this gap by documenting wet conditions in the interior during the landfall of two ARs. More recently, Rutz and Steenburgh (2012) show the important role of landfalling ARs across Baja California (hereinafter, Baja) on the annual precipitation in Arizona.

The study presented here provides the first detailed case study to test the hypothesis that an AR can penetrate inland from the Pacific Ocean to central Arizona and generate extreme rainfall and flooding in that semiarid region of the United States. It also highlights the fact that wintertime ARs can incur significant societal impacts across the desert Southwest. Historically, although devastating droughts have challenged societies there since at least the time of the Anasazi, floods are believed to have caused the demise of one of the most populous and productive societies of the pre-Spanish era, the Hohokam people of the Salt and Gila Rivers area in central Arizona (Calloway 2003). Since most of the top 10 discharges on the Salt and Gila Rivers in the last ~90 years have occurred between November and March (data available at <http://waterdata.usgs.gov/az/>

nwis/rt), it is plausible that many of the floods leading to the Hohokam's demise could have been caused by winter storms, including inland-penetrating ARs of the sort studied here.

In late January 2010, a series of transient baroclinic waves impacted the southwestern United States. Six consecutive 24-h gridded precipitation analyses spanning the period 1200 UTC 18 January to 1200 UTC 24 January (Fig. 1) show the greatest accumulations across California and Arizona. The last of these storms, on 21–22 January, was by far the strongest, and it produced widespread heavy rains, record-setting high-elevation snows and blizzard conditions, strong thunderstorms, flash flooding, damaging winds, dust storms, power outages, and road closures across Arizona. Like many other stations across the southwestern United States, Phoenix recorded its lowest-ever pressure reduced to sea level (i.e., 988.8 hPa) during this storm, which caused three fatalities and more than \$11 million in damages across the state (NCDC 2010). Part I of this study, presented here, will demonstrate that the powerful trailing wave brought intense AR conditions from the coast into the semiarid interior of Arizona (see Fig. 2 for the domain of interest) and that the orographic and hydrometeorological responses during this event were comparable to what occurs when ARs make landfall along the west coasts of continents (see references above). Part II of this study (M. Hughes et al. 2013, unpublished manuscript) will utilize high-resolution simulations of this storm to investigate water vapor pathways directed from the Pacific coast into the interior.

## 2. Gridded datasets and observing systems

Two global gridded datasets from the National Oceanic and Atmospheric Administration's (NOAA) National Centers for Environmental Prediction (NCEP) provided synoptic-scale context for this study: 1) the Climate Forecast System Reanalysis (CFSR) package, used for plan-view and cross-section analyses, and 2) the Global Data Assimilation System (GDAS) package, used for back-trajectory analyses. The CFSR analyses (Saha et al. 2010) are available every 6 h (starting at 0000 UTC) at  $0.5^\circ \times 0.5^\circ$  horizontal resolution with 37 levels starting in 1979. Normalized anomaly fields from the CFSR were generated by employing the method of Hart and Grumm (2001) and using a baseline climatology between 1979 and 2008. The GDAS analyses are available every 6 h with  $1.0^\circ$  horizontal resolution; the vertical resolution is 25 hPa between 1000 and 900 hPa and 50 hPa aloft. Backward air parcel trajectories were computed from the GDAS analyses using the Hybrid Single-Particle Lagrangian Integrated

## 24-h gridded precipitation analysis

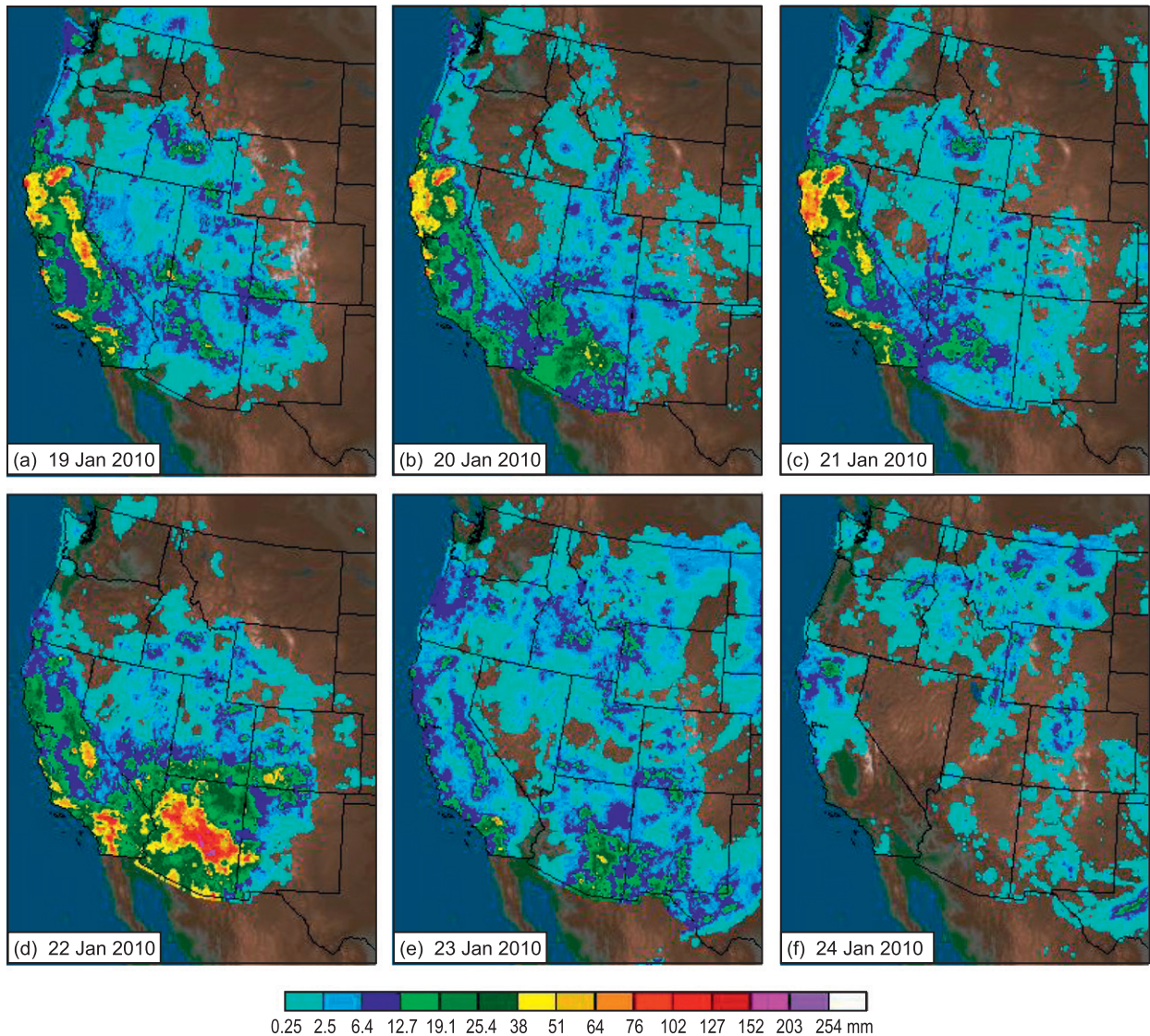
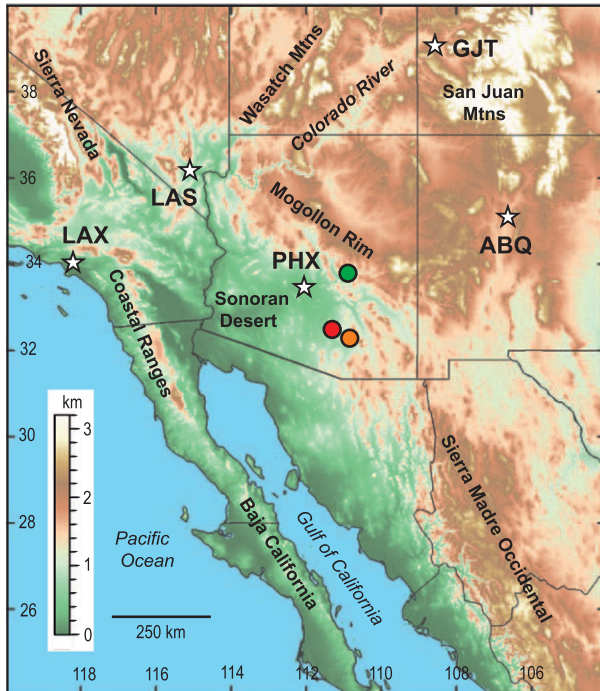


FIG. 1. Western United States 24-h quantitative precipitation estimation (mm) from the Advanced Hydrological Prediction Services ending 1200 UTC (a) 19, (b) 20, (c) 21, (d) 22, (e) 23, and (f) 24 Jan 2010.

Trajectory (HYSPLIT) model (Draxler and Hess 1997; Draxler and Rolph 2011).

NOAA's Climate Prediction Center (CPC) developed and maintains the unified precipitation dataset (UPD) at  $0.25^\circ$  horizontal resolution (e.g., Higgins et al. 2007). The domain is bounded by  $20^\circ$ – $50^\circ$ N latitude and  $130^\circ$ – $55^\circ$ W longitude. The UPD is derived from three sources: NOAA's daily co-op stations (1948 to present), CPC's dataset (1992 to present), and daily accumulations from hourly precipitation observations (1948 to present). The time period of record utilized for the current analysis is 1 January 1970 through 31 December 2010.

Integrated water vapor (IWV) retrievals were collected from the Special Sensor Microwave Imager/Sounder (SSMIS) observing platform on board the *FI6* and *FI7* Defense Meteorological Satellite Program polar orbiting satellites. The IWV was retrieved using the Wentz (1995) optimal statistical algorithm. These data, which have a native horizontal resolution of  $\sim 40$  km in  $\sim 1400$ -km-wide swaths, were placed on a  $\sim 25$ -km-resolution grid and combined into twice-daily composite images corresponding to the time intervals between 0000 and 1159 UTC (i.e., morning) and 1200 and 2359 UTC (i.e., afternoon). Reliable SSMIS IWV retrievals are



- Tucson 449 MHz wind profiler: 32.51N/111.34W/578m MSL
- Tucson GPS IWV: 32.23N/110.95W/724m MSL;
- Tucson rawinsonde: 32.23N/110.96W/753m MSL;
- Tucson surface met. site: 32.13N/110.96W/778m MSL;
- Marshall Gulch precip. gauge: 32.42N/110.75W/2171m MSL
- Workman Creek SNOTEL: 33.81N/110.91W/2103m MSL

FIG. 2. Regional terrain base map of the southwestern United States. Key observing sites are included on the map (see also the legend), as are selected cities (LAX: Los Angeles, CA; LAS: Las Vegas, NV; PHX: Phoenix, AZ; ABQ: Albuquerque, NM; GJT: Grand Junction, CO).

confined to oceanic regions where surface microwave emissivity is weak. We also utilized  $\sim 10$ -km resolution,  $10.7\text{-}\mu\text{m}$  channel infrared (IR) imagery from the *Geostationary Operational Environmental Satellite 11* (GOES-11).

A NOAA 449-MHz radar wind profiler (White et al. 2007; NOAA 2007) was deployed for the U.S. Army northwest of Tucson, Arizona, at an altitude of 578 m above mean sea level (MSL) (Fig. 2) and provides hourly averaged vertical profiles of horizontal wind from 0.2 to 8.0 km above ground with  $\sim 200$ -m vertical resolution. Wind observations were edited objectively using the time–height continuity method of Weber et al. (1993). The height of the precipitation melting level was obtained hourly using the objective brightband detection method of White et al. (2002); the melting level typically resides  $\sim 200$  m below the  $0^\circ\text{C}$  freezing level (Stewart et al. 1984; White et al. 2002). A dual-channel

GPS receiver, located 48 km southeast of the wind profiler at an altitude of 724 m MSL (Fig. 2), provides 30-min measurements of IWV in the full atmospheric column with  $\sim 1$  mm accuracy (Duan et al. 1996; Mattioli et al. 2007). Operational data collected within  $\sim 5$  km of the Tucson GPS receiver were also used: twice-daily rawinsonde profiles of wind velocity and thermodynamics and hourly surface meteorological data.

Regional analyses were carried out using data from several national networks. NOAA's National Weather Service Cooperative Observer Program (COOP) gathers observations from a dense network of volunteers who report daily maximum and minimum temperatures and precipitation. The U.S. Department of Agriculture's Natural Resources Conservation Service manages a network of automatic hourly resolution snow monitoring stations (referred to as snow telemetry sites, or SNOTEL for short; e.g., Trabant and Clagett 1990) with accompanying precipitation gauges across the western United States. Snow pillows at these sites measure the weight of the snow water equivalent (SWE) of the snowpack. Because of quality-control issues on subdaily time scales, only the daily averaged SWE and precipitation measurements are used here. Finally, the Department of the Interior's U.S. Geological Survey (USGS) maintains a nationwide network of gauges on streams and rivers.

### 3. Synoptic-scale evolution overview

In this section we present a synoptic-scale overview of the baroclinic wave train that impacted Arizona between 18 and 22 January 2010. A sequence of four SSMIS satellite images (Figs. 3a–d) highlights the IWV evolution over the northeastern Pacific during this period, when three ARs made landfall (labeled AR 1, 2, and 3) along the California and Baja coast. Each disturbance was tied to baroclinic wave development along a zonally oriented quasi-stationary polar cold-frontal boundary (this boundary is best visualized in Figs. 5e and 8e from section 4). The IWV plumes in ARs 1 and 3 extended from the tropical water vapor reservoir over the central Pacific, but water vapor content increased significantly along the ARs in the midlatitudes, well beyond the tropics, because of upward sea surface latent-heat fluxes and/or frontal dynamics that helped draw extratropical water vapor into the ARs. In particular, the IWV core of AR 3 increased from about 3 cm to more than 4 cm in the 24-h period ending on the afternoon of 21 January 2010 as its tropical connection diminished (Figs. 3c,d). The large IWV content in the core of AR 3 compared to the preceding ARs reflects the relative strength of this concluding storm, which severely impacted Arizona on 21–22 January 2010.

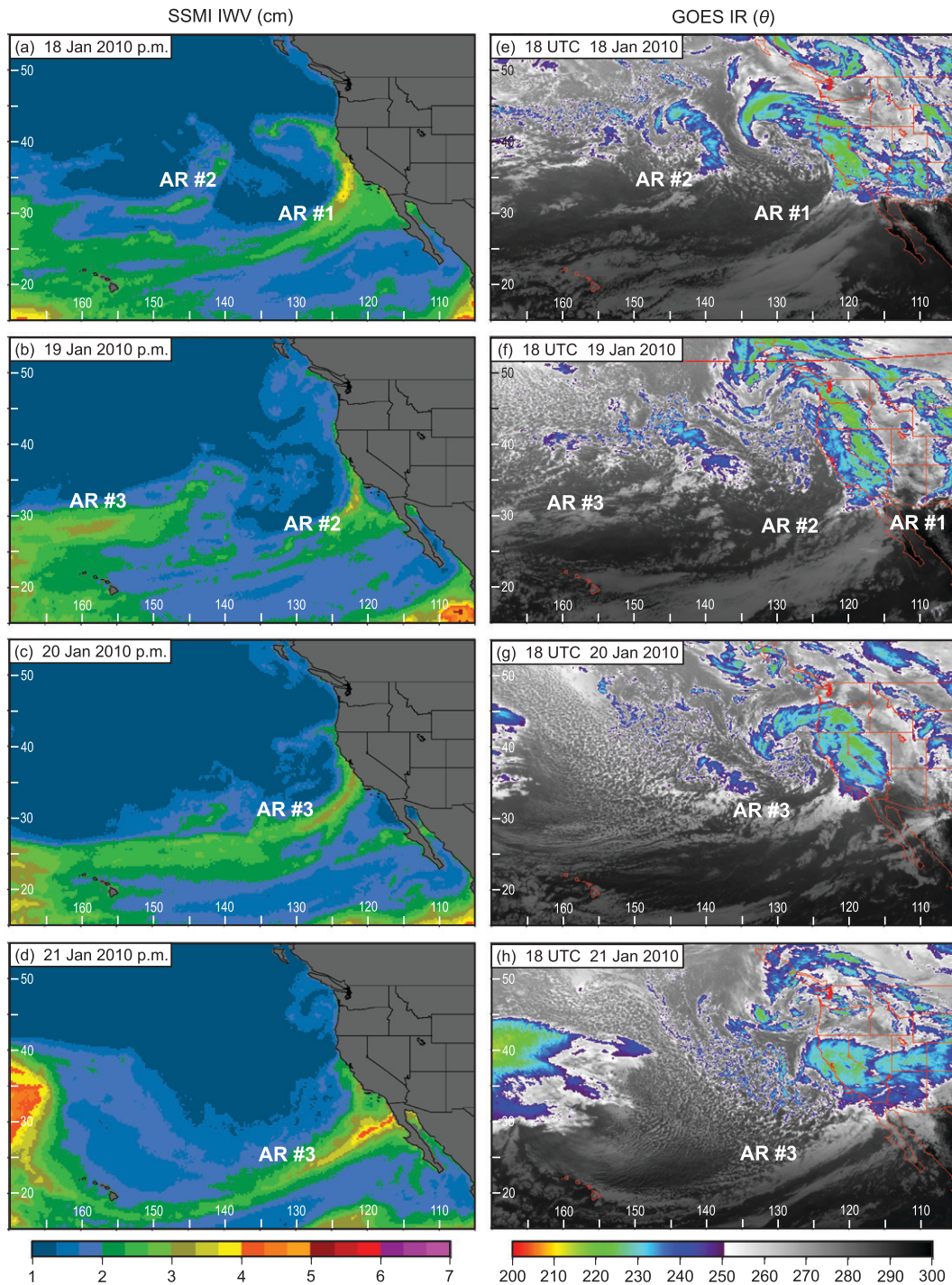


FIG. 3. Composite SSMIS satellite imagery of IWV (cm; color bar at bottom) constructed from polar-orbiting observation swaths between  $\sim 1200$  and 2359 UTC on (a) 18, (b) 19, (c) 20, and (d) 21 Jan 2010. *GOES-II* 10.7- $\mu\text{m}$  channel (i.e., infrared) satellite imagery of brightness temperature (K) at 1800 UTC on (e) 18, (f) 19, (g) 20, and (h) 21 Jan 2010. Three distinct AR events are annotated.

*GOES* satellite imagery at 1800 UTC on 18–21 January 2010 provides an IR cloud-top temperature perspective of the sequence of landfalling storms (Figs. 3e–h). The three ARs are indistinct compared to their depiction in

the SSMIS imagery, with quasi-organized but shallow cloud bands coinciding with the ARs over the Pacific. The lack of deep clouds in the ARs offshore, which has also been noted previously (Ralph et al. 2004; Neiman

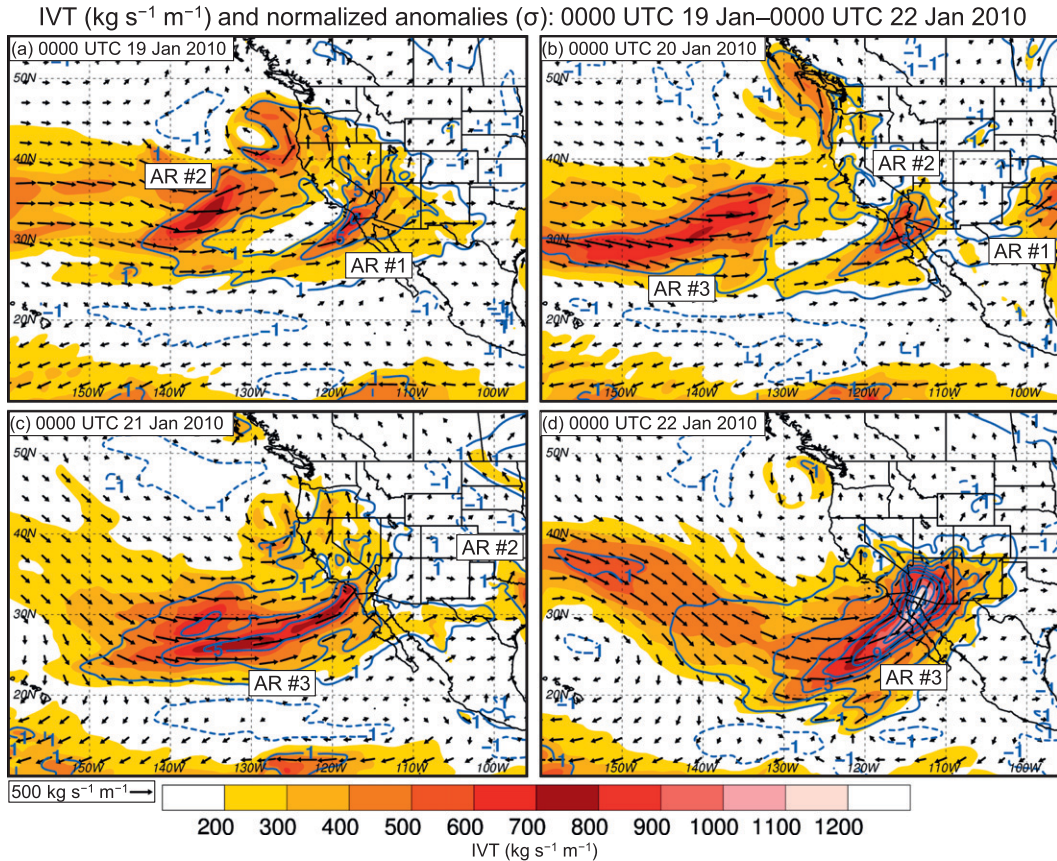


FIG. 4. The 1000–300-hPa IVT [ $\text{kg s}^{-1} \text{m}^{-1}$ ; color fill with vectors overlaid (scales shown)] and IVT normalized anomalies (nonzero standard deviations with  $2\sigma$  interval; solid contours for  $\sigma \geq 1$  and dashed for  $\sigma = -1$ ) from the 0.5°CFSR dataset at 0000 UTC (a) 19, (b) 20, (c) 21, and (d) 22 Jan 2010. Three distinct AR events are annotated.

et al. 2008a), likely reflects a relatively shallow frontal circulation over the open waters. In contrast, the IR imagery contains organized cold (i.e., deep) cloud tops in the comma-head region of each landfalling storm where broad large-scale lift typically occurs. Interestingly, based on the IR imagery alone, the extratropical cyclone of AR 3 does not appear substantially different than its predecessors, despite the fact that this was the strongest and most impactful of the three storms. However, the SSMIS satellite imagery, and the vapor-transport analyses that follow, reveal otherwise.

Figure 4 shows the vertically integrated 1000–300 hPa horizontal water vapor flux [integrated vapor transport (IVT); see Neiman et al. (2008b) for calculation methodology] at 24-h intervals starting at 0000 UTC 19 January 2010; normalized IVT anomalies are also included. At 0000 UTC 19 January (Fig. 4a), AR 1 was impacting Southern California and the desert Southwest with core values of northeastward-directed IVT ranging between 400 and  $800 \text{ kg s}^{-1} \text{m}^{-1}$  and 3–7 standard deviations ( $\sigma$ ) above normal. Farther west, AR 2 was beginning

to strengthen in response to cyclogenesis offshore (not shown). One day later (Fig. 4b), the IVT signature of AR 1 decayed as it migrated eastward over the Great Plains, while AR 2 strengthened (at least from a normalized anomaly perspective) as it organized and also made landfall in Southern California. Farther west, AR 3 began consolidating into a zonally oriented corridor of enhanced IVT ( $\sim 500 \text{ kg s}^{-1} \text{m}^{-1}$ ) during the initial stage of a new, strong cyclogenesis event (not shown). By 0000 UTC 21 January (Fig. 4c), AR 2 had moved rapidly inland and dissipated, while the IVT maximum of AR 3 intensified to  $\sim 700 \text{ kg s}^{-1} \text{m}^{-1}$  and 3–5  $\sigma$  above normal as it approached Southern California. The cyclonic curvature of the IVT field in the vicinity of AR 3 amplified from 24 h earlier in response to deep-tropospheric cyclogenesis (not shown). Cyclonic amplification and AR intensification persisted for an additional 24 h through 0000 UTC 22 January (Fig. 4d). At this later time, exceptionally strong IVTs exceeded  $1200 \text{ kg s}^{-1} \text{m}^{-1}$  and impinged on Arizona from the southwest. These magnitudes are far larger

than the largest IVTs in the 30-yr CFSR dataset near Arizona; hence, normalized anomalies exceed  $13\sigma$ . More generally, the IVTs in the core of AR 3 represent the upper end of values observed previously in ARs over the northeastern Pacific (e.g., Ralph et al. 2004, 2005, 2011; Neiman et al. 2008a,b, 2011). Notably, the extreme IVT intensification occurred without poleward entrainment of tropical water vapor. The remainder of this study will focus on the dynamical and hydrometeorological characteristics of AR 3.

#### 4. Dynamical analysis of the flood-producing AR

Using the global gridded datasets described earlier, section 4 highlights key dynamical characteristics of AR 3 during its crucial 12-h phase of landfall and inland penetration between 1200 UTC 21 January and 0000 UTC 22 January 2010. In general, these characteristics mirror those of high-impact ARs affecting the West Coast states, save for the fact that some (though not all) of those coastal ARs exhibit a pronounced linkage with the tropics.

##### a. 1200 UTC 21 January 2010

Figure 5 provides a plan-view perspective at 1200 UTC 21 January 2010 as AR 3 began making landfall. Core values of northeastward-directed IVT exceeded  $1000 \text{ kg s}^{-1} \text{ m}^{-1}$  west of Baja (Fig. 5a) and represented a  $>40\%$  increase in magnitude from 12 h earlier. The leading edge of this IVT plume penetrated inland across southern Arizona. Companion analyses at 850 hPa (Figs. 5b,c) show large mixing ratios ( $6\text{--}10 \text{ g kg}^{-1}$ ) within a corridor of strong pre-cold-frontal southwesterly flow ( $\sim 25 \text{ m s}^{-1}$ ), thus highlighting the presence of enhanced low-level water vapor transport in the AR to the south of a developing cyclone offshore of California. An organized region of 850-hPa frontogenesis (derived from the Petterssen two-dimensional frontogenesis equation; Petterssen 1956) was aligned parallel to the strengthening AR and contributed to the concentration of water vapor. Persistent upward sea surface latent-heat fluxes of  $50\text{--}200 \text{ W m}^{-2}$  along the AR over the Pacific and Gulf of California (Fig. 5d), which were bolstered by areal-averaged sea surface temperature anomalies of  $\sim 0.4\text{--}0.8^\circ\text{C}$  during a warm phase of El Niño–Southern Oscillation (ENSO) (i.e., multivariate ENSO index = 1.0–1.5; Wolter and Timlin 1998), provided additional water vapor (e.g., Newman et al. 2012). Farther south, dry air at 850 hPa ( $<4 \text{ g kg}^{-1}$ ) separated the AR from the tropical water vapor reservoir, while cold advection in northwesterly flow occurred poleward of the AR. The freezing level (Fig. 5e) was at high altitudes ( $>3 \text{ km MSL}$ ) in the core of the AR, consistent with previous AR studies (e.g.,

Neiman et al. 2008a,b; Ralph et al. 2011). The northeast quadrant of Arizona exhibited low freezing levels ( $<1 \text{ km MSL}$ ) in the wake of the departing extratropical cyclone associated with AR 2, while the freezing level in the southwest corner of the state rebounded to  $\sim 2.8 \text{ km MSL}$  in strong warm advection during the initial landfall of AR 3. The tight freezing-level gradient across the southern United States and over the Pacific marks the strong midtropospheric temperature gradient associated with the baroclinic wave train that impacted the semi-arid desert Southwest. At 500 hPa (Fig. 5f), a deep trough with geopotential heights  $3\text{--}5 \sigma$  below normal, and strong cyclonic vorticity advection (CVA) indicative of quasigeostrophic ascent (given the assumption CVA increased with height), impinged on the strengthening AR just offshore. The landfalling AR was positioned beneath the right exit quadrant of a  $\sim 90 \text{ m s}^{-1}$  polar jet at 250 hPa (Fig. 5g), which, for a straight jet, favors synoptic subsidence (e.g., Beebe and Bates 1955). In a cyclonically curved jet, such as what occurred here, the subsident cell is typically weaker and shifted equatorward but would have still been located over the AR, thus highlighting the vertical decoupling of upper-tropospheric dynamical forcing at this stage of AR development.

Key characteristics through AR 3 are highlighted in four cross sections (Fig. 6; baseline NW–SE in Fig. 5). The potential temperature ( $\theta$ ), along-AR isotachs, and potential vorticity (PV) fields (Fig. 6a) show a region of large lower-stratospheric PV located on the cyclonic-shear side of the  $90 \text{ m s}^{-1}$  polar jet at  $\sim 250 \text{ hPa}$ ; the PV enters the troposphere within the stable stratification and enhanced vertical and cyclonic shear of the equatorward-descending tropopause fold and polar cold front. A secondary, shallower zone of enhanced baroclinicity resides below 600 hPa in the center of the cross section in an area of strong ( $>25 \text{ m s}^{-1}$ ) low-level west-southwesterly flow, and it corresponds to the 850-hPa frontal zone and enhanced water vapor band in Figs. 5b,c. The secondary baroclinic zone is much more pronounced in an analysis of equivalent potential temperature ( $\theta_e$ ; Fig. 6b), where it extends upward from the ocean surface to the upper cold front and associated PV anomaly. To its southeast, a plume of high- $\theta_e$  air ( $>324 \text{ K}$ ) with moist neutral stability penetrated vertically to  $\sim 650 \text{ hPa}$  and was accompanied by a focused, shallow band of water vapor flux convergence that likely contributed to the enhancement of water vapor and its transport within this strong AR. Quasi-saturated conditions (i.e., relative humidity  $>80\%$ ) were observed beneath the polar cold front aloft. The  $\theta_e$  field is also shown with in-plane vectors (Fig. 6c), which reveals two regions of organized ascent: a shallow plume exceeding  $-10 \mu\text{b s}^{-1}$  in the high- $\theta_e$  air at the leading edge of the moist baroclinic frontal zone,

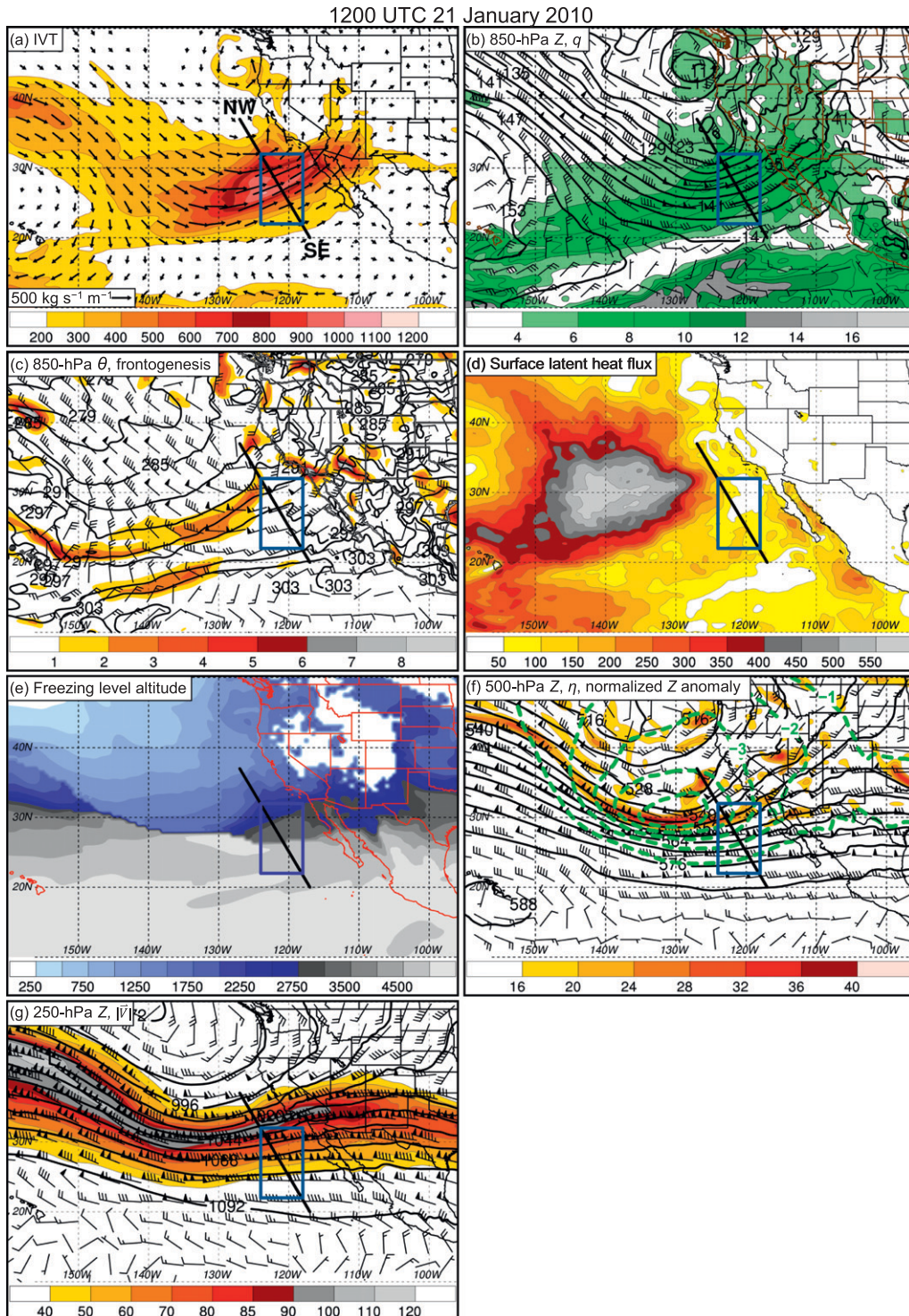


FIG. 5. Plan-view plots at 1200 UTC 21 Jan 2010 from the 0.5°CFSR dataset: (a) 1000–300-hPa IVT ( $\text{kg s}^{-1} \text{m}^{-1}$ ; color fill with vectors overlaid); (b) 850-hPa geopotential height (dam; black contours), water vapor mixing ratio ( $\text{g kg}^{-1}$ ; green fill), and wind velocities (flags =  $25 \text{ m s}^{-1}$ , barbs =  $5 \text{ m s}^{-1}$ , half barbs =  $2.5 \text{ m s}^{-1}$ ); (c) 850-hPa potential temperature (K; black contours), frontogenesis [ $\text{K (100 km)}^{-1} (24 \text{ h})^{-1}$ ], and wind velocities; (d) surface latent-heat flux ( $\text{W m}^{-2}$ ; color fill); (e) freezing-level altitude (meters; color fill); (f) 500-hPa geopotential height (dam; black contours), absolute vorticity ( $10^{-5} \text{ s}^{-1}$ ; color fill), normalized height anomalies ( $\sigma > 0$ ; green dashed contours), and wind velocities; and (g) 250-hPa geopotential height (dam; black contours), isotachs ( $\text{m s}^{-1}$ ; color fill), and wind velocities. The black line labeled NW–SE in (a) and shown in all panels is a projection line for the cross section in Fig. 6. The blue rectangle in each panel shows the domain for a  $4 \times 6$  array of back-trajectory endpoints in Fig. 7.

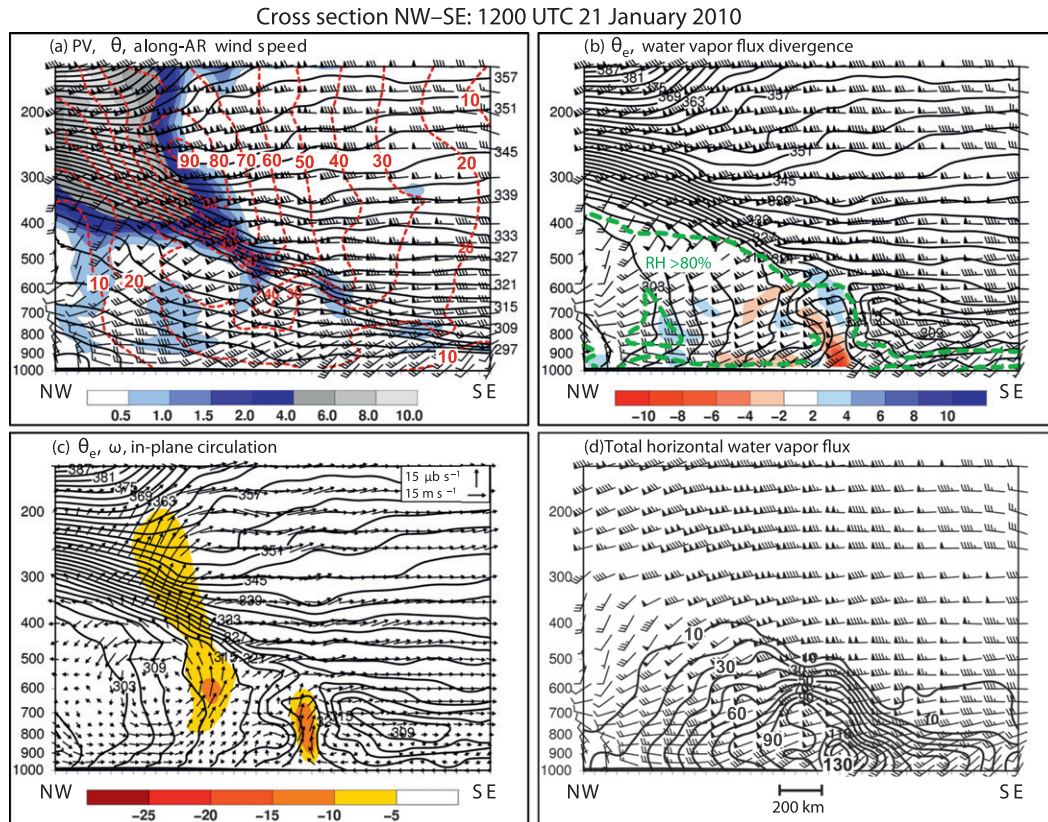


FIG. 6. Cross-section plots along line NW–SE in Fig. 5 at 1200 UTC 21 Jan 2010 from the  $0.5^\circ$  CFDS dataset: (a) potential temperature (K; black contours at 3-K interval), along-AR isotachs ( $\text{m s}^{-1}$ ; directed from  $240^\circ$ , i.e., approximately into the page; red dashed), and potential vorticity ( $10^{-6} \text{ m}^2 \text{ s}^{-1} \text{ K kg}^{-1}$ ; color fill); (b) equivalent potential temperature (K; black contours at 3-K interval), water vapor flux divergence [ $\text{g kg}^{-1} (24 \text{ h})^{-1}$ ]; color fill], and relative humidity of 80% (green dashed); (c) equivalent potential temperature (K; black contours), ascent ( $\mu\text{b s}^{-1}$ ; color fill), and in-plane circulation vectors; and (d) horizontal water vapor flux ( $\text{kg s}^{-1} \text{ m}^{-1}$ ; black contours). Wind velocities in (a),(b), and (d) are described in Fig. 5b.

and a much deeper but weaker plume tied to the PV anomaly aloft. The lateral offset of these plumes highlights the decoupling of the low-level and upper-level dynamics at this time. The final cross-section panel (Fig. 6d) clearly defines the AR with its very strong water vapor fluxes in the lower and middle troposphere. The core magnitude of the AR ( $110\text{--}130 \text{ kg s}^{-1} \text{ m}^{-1}$ ), which surpasses previously published cases by 30%–60% (Ralph et al. 2004, 2011), was situated on the equatorward side of the moist baroclinic frontal zone beneath the PV-rich polar cold front and tropopause fold aloft.

To further quantify the transport of water vapor in AR 3, a Lagrangian approach was employed by computing a  $4 \times 6$  array of HYSPLIT 84-h backward air parcel trajectories ending at 1200 UTC 21 January 2010 at an altitude of 2 km MSL within the domain bounded by  $22^\circ\text{--}32^\circ\text{N}$  and  $124^\circ\text{--}118^\circ\text{W}$  (Fig. 7; blue rectangle in Fig. 5). The parcels were clustered into three subdomains: the poleward side of the AR (blue), within the

AR (green), and the equatorward side (red). All three clusters extended quasi-zonally across the Pacific poleward of  $20^\circ\text{N}$ , exhibiting anticyclonic curvature near the date line and then cyclonic curvature once approaching the coast (Fig. 7a). Companion back trajectories ending at 1 and 3 km MSL were similar (Fig. 7a). None of the back trajectories originated from the tropical water vapor reservoir (whose poleward terminus remained south of  $15^\circ\text{N}$ ), despite the fact that the IWV within AR 3 increased markedly between  $\sim 1800$  UTC 20–21 January (Figs. 3c,d) and the corresponding IVT strengthened significantly. Physical insight into the AR evolution can be gleaned by averaging the three clusters of eight trajectories (Figs. 7b–d). All three clusters experienced significant subsidence exceeding 100 hPa along most of their averaged paths, while only the two northern clusters ascended in the mean (by  $\sim 80\text{--}100$  hPa) during their final 18–24 h because of their proximity to frontally forced ascent (e.g., Figs. 5c, 6c) and midtropospheric CVA (Fig. 5f).

## 84-h Hysplit back trajectories at 12 UTC 21 January 2010

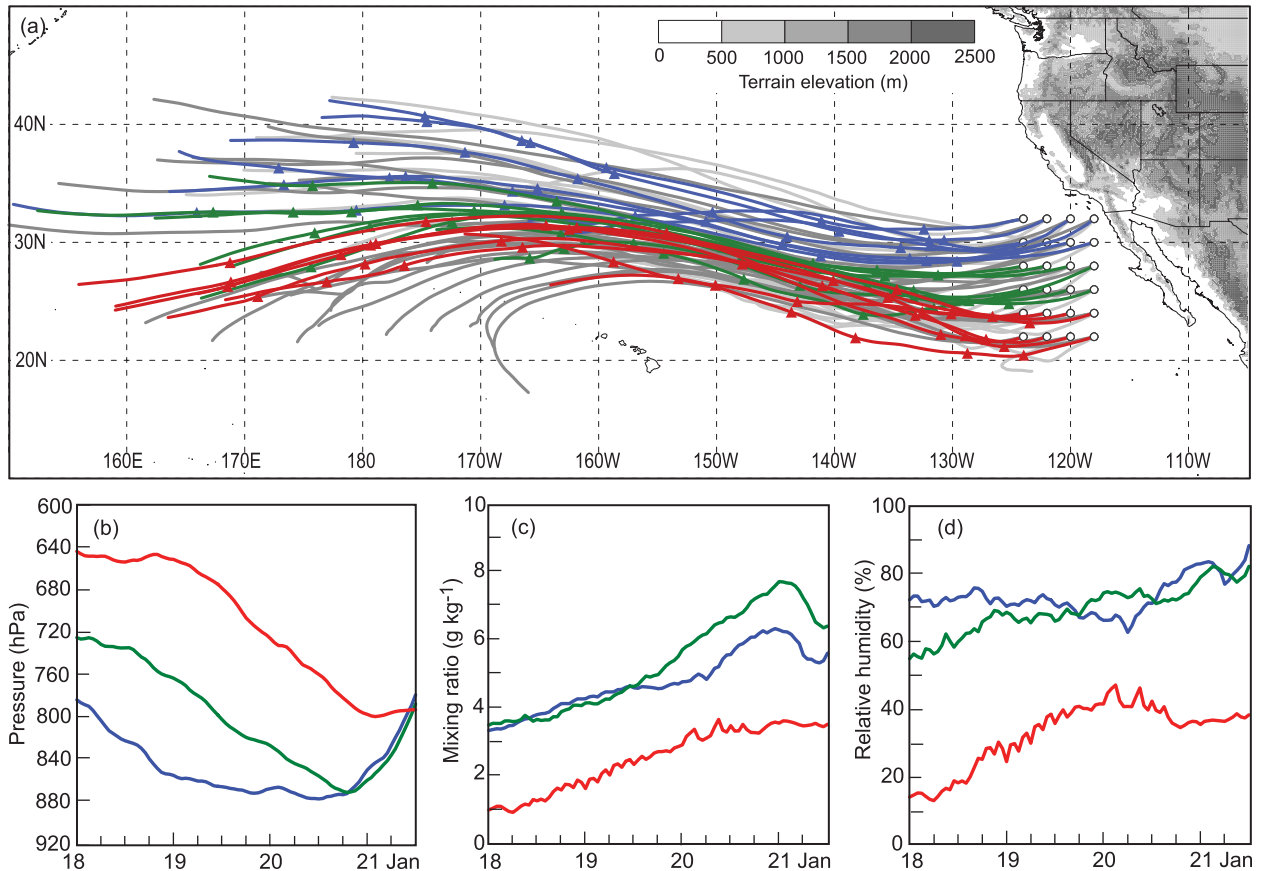


FIG. 7. (a) A  $4 \times 6$  array of 84-h backward air parcel trajectories ending at 1200 UTC 21 Jan 2010 (white circles) at 1 km MSL (light gray), 2 km MSL (colored, with triangles), and 3 km MSL (medium gray), computed from the GDAS analyses using the HYSPLIT model. The 2-km trajectories are color coded based on their latitude endpoints (blue is northernmost, green is middle, and red is southernmost), and the accompanying triangles mark the air parcel positions at 12-h increments backward from the end time. Terrain elevation (meters) is shaded. (b) Time series of average hourly air pressure (hPa) along the three sets of colored trajectories shown in (a), from 0000 UTC 18 Jan through 1200 UTC 21 Jan 2010. (c) As in (b), but for water vapor mixing ratio ( $\text{g kg}^{-1}$ ). (d) As in (b), but for relative humidity (%).

All three clusters gained water vapor during parcel descent. Processes that can account for this moistening include confluent flow (though not convergent flow, which would yield ascent), evaporation from precipitation, and evaporation from the sea surface (unlikely, given the initially high altitude of the parcels). In the final 12 h, the two northern parcel clusters lost  $\sim 17\%$  of their peak water vapor content, likely in response to condensation and rainout (observed by SSMIS; not shown) during ascent (mean relative humidities during this period exceeded 80%). The southernmost cluster was the driest in both relative and absolute terms, thus further highlighting the fact that the strong AR did not originate in the tropics over the northeastern Pacific.

#### b. 0000 UTC 22 January 2010

The evolution of the synoptic environment and embedded AR was gauged by comparing the six-panel

analyses at 0000 UTC 22 January 2010 (Fig. 8) with their counterparts 12 h earlier (Fig. 5). By 0000 UTC 22 January, the northeastward-directed AR had penetrated deep into the desert Southwest, and the IVT within its core increased by an additional 20% to  $>1200 \text{ kg s}^{-1} \text{ m}^{-1}$  (Fig. 8a). At 850 hPa, the AR was still defined by a narrow, frontogenetic band of large mixing ratios within strong pre-cold-frontal southwestward flow (Figs. 8b,c) that increased to  $\sim 30 \text{ m s}^{-1}$ . The wedge of dry air between the AR and tropical water vapor reservoir began to erode to the southwest of southern Baja, and collocated IVTs were strengthening at the southern periphery of the AR south of 20°N near 120°W, thus suggesting an initial entrainment of tropical water vapor. However, these tropical air parcels remained south of Arizona. Upward sea surface latent-heat fluxes into the AR persisted until landfall (Fig. 8d), during which the parent cyclone at 850 hPa came ashore

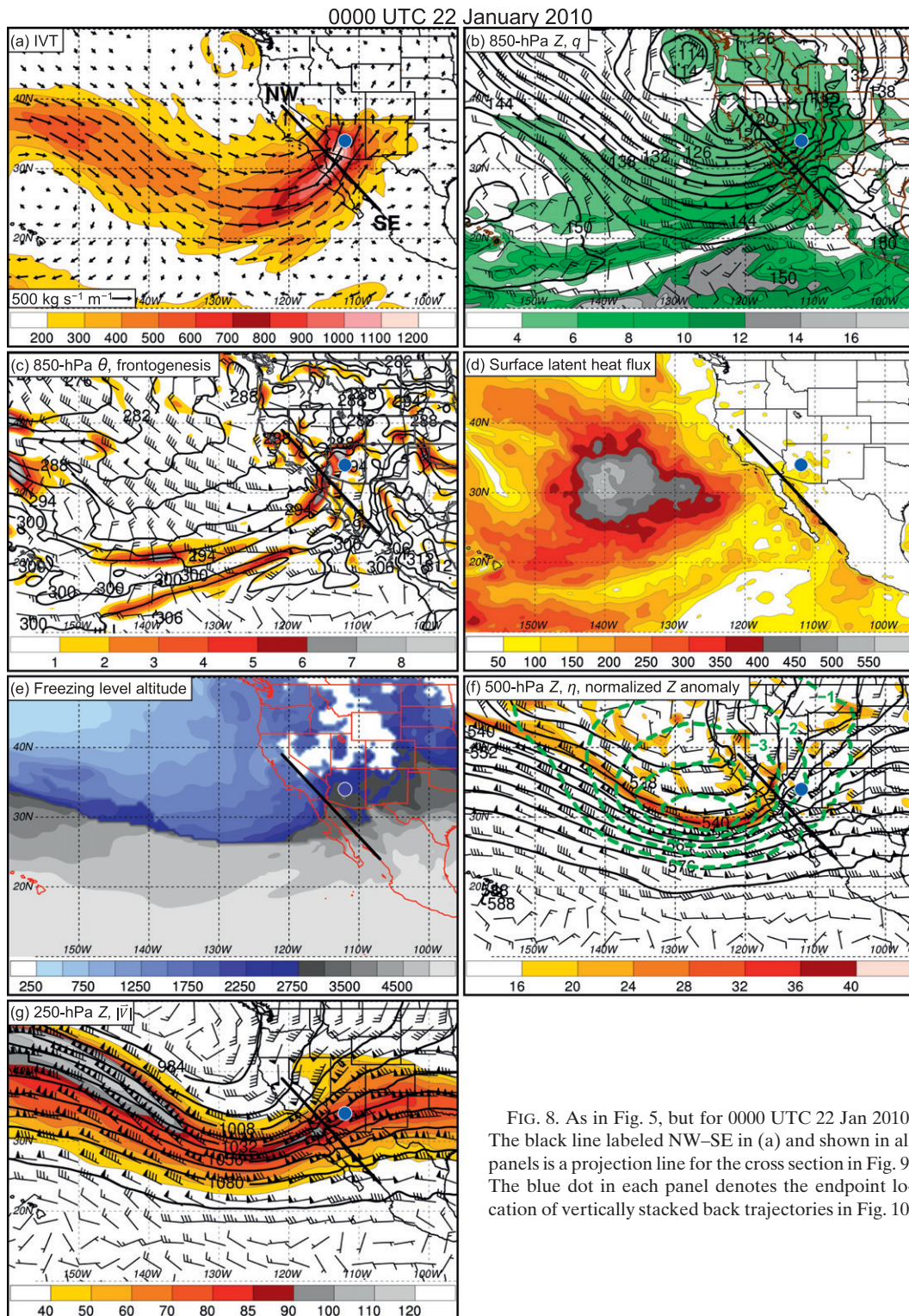


FIG. 8. As in Fig. 5, but for 0000 UTC 22 Jan 2010. The black line labeled NW-SE in (a) and shown in all panels is a projection line for the cross section in Fig. 9. The blue dot in each panel denotes the endpoint location of vertically stacked back trajectories in Fig. 10.

across northern California. The freezing-level altitude increased markedly across central Arizona in 12 h, reaching  $\sim 2.8$  km MSL by 0000 UTC 22 January (Fig. 8e) in response to strong warm advection with the approach

of the AR. Aloft, the intense trough at 500 hPa approached the coast (Fig. 8f), while, downwind, CVA and diffluent flow enveloped Arizona during the inland penetration of the intense AR across the state. The

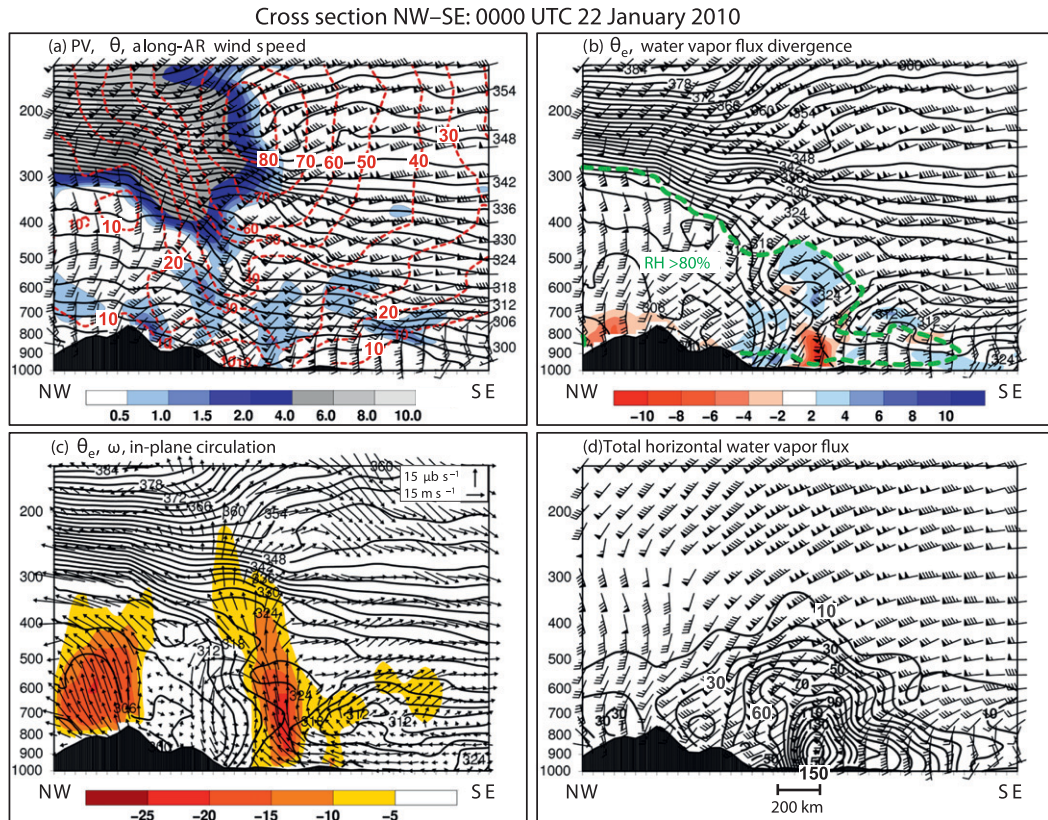


FIG. 9. As in Fig. 6, but along line NW–SE in Fig. 8 at 0000 UTC 22 Jan 2010. The along-AR isotachs in (a) are directed from  $230^\circ$ , that is, approximately into the page.

vertical phasing of the AR with the upper-level dynamics is highlighted at 250 hPa (Fig. 8g), where the exit nose of the cyclonically curved polar jet, a favored region of ascent (Beebe and Bates 1955), sagged southward across central and northern Arizona above the downwind terminus of the AR.

Cross sections through the landfalling AR at 0000 UTC 22 January are presented in Fig. 9 (baseline NW–SE in Fig. 8). The lower-stratospheric PV anomaly remained anchored on the cyclonic-shear side of the polar jet at  $\sim 250$  hPa (Fig. 9a). In the troposphere, frontogenesis (e.g., Fig. 8c) steepened and deepened the dry and moist cold-frontal isentropes and sharpened the cross-front wind shift (Figs. 9a,b) relative to 12 h earlier. Strong low-level southwesterly flow exceeded  $35 \text{ m s}^{-1}$  in the prefrontal AR corridor of weakly stratified, high- $\theta_e$  air (320–324 K), where the water vapor flux convergence strengthened significantly in 12 h (Fig. 9b). The lateral phasing of the PV anomaly aloft with the intensifying low-level cold front yielded a vertically coupled plume of strong ascent spanning the depth of the troposphere within the AR as it approached Arizona (Fig. 9c). The strongest upward motion ( $-15$  to  $-25 \mu\text{b s}^{-1}$ ), which

increased in magnitude by a factor of 2 from 12 h earlier, was situated between 900 and 650 hPa. The lower half of this layer intersected the high Mogollon Rim of central Arizona and, combined with extreme orographic forcing there (see section 5a), produced record precipitation and runoff. A companion cross section of water vapor fluxes (Fig. 9d) pinpoints the AR's location in the ascending pre-cold-frontal airstream. The already large lower-tropospheric values at 1200 UTC 21 January increased to  $>150 \text{ kg s}^{-1} \text{ m}^{-1}$  in a narrowing filament associated with strong low-level frontogenesis; the vapor transport within the AR was directed orthogonal to the Mogollon Rim.

Figure 10 shows a trio of vertically stacked 132-h backward air parcel trajectories ending at 1, 2, and 3 km MSL in the AR over central Arizona at 0000 UTC 22 January. Unlike the 84-h trajectories that terminated in and near the AR offshore 12 h earlier (Fig. 7), these have much shorter trans-Pacific pathways despite the fact that they span two additional days. These latter trajectories also remained north of  $20^\circ\text{N}$  and poleward of the tropical water vapor reservoir. The two lower trajectories remained near the sea surface

## 132-h Hysplit back trajectories ending at 00 UTC 22 January 2010

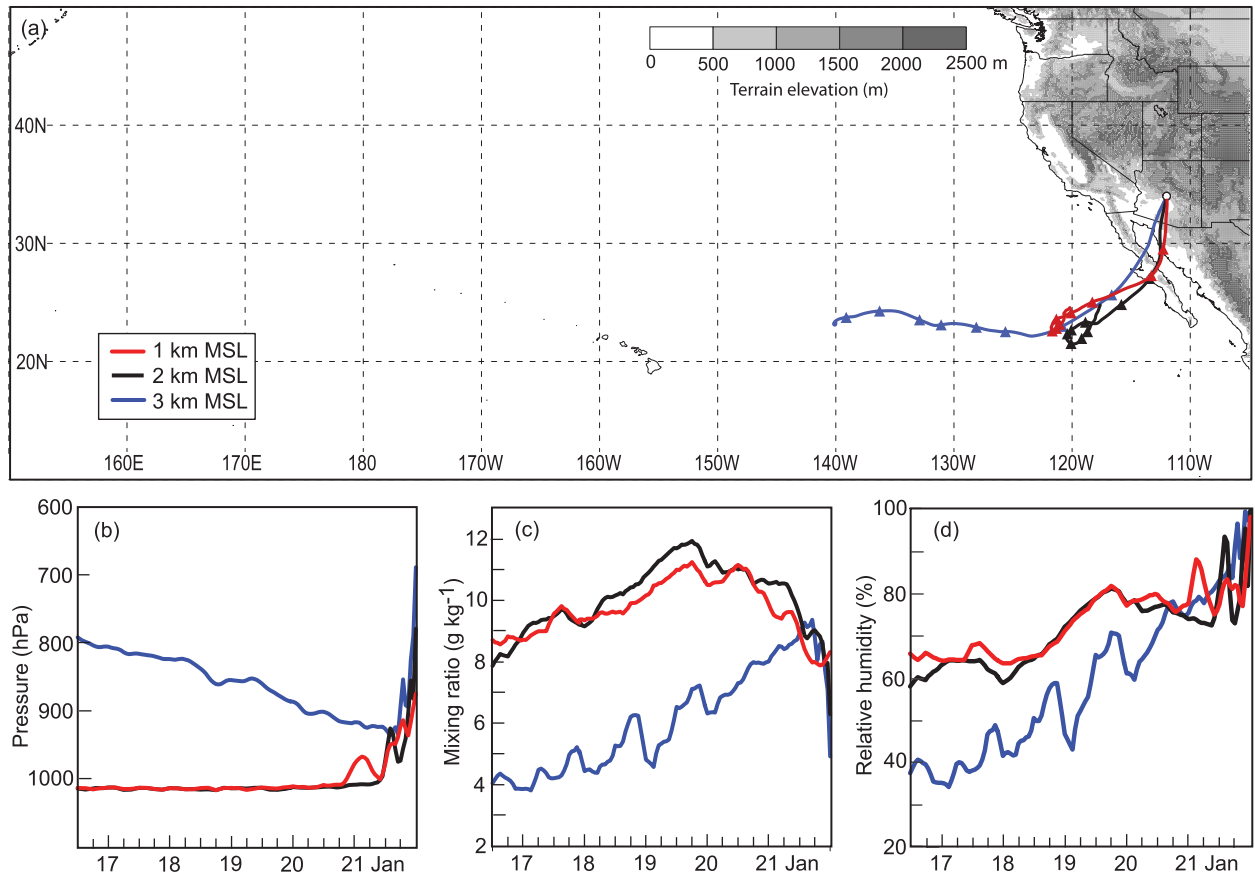


FIG. 10. A trio of 132-h backward air parcel trajectories ending at 0000 UTC 22 Jan 2010 at 1, 2, and 3 km MSL (red, black, and blue, respectively), computed from the GDAS analyses using the HYSPLIT model. The triangles mark the air parcel positions at 12-h increments backward from the end time. Terrain elevation (m) is shaded. (b) Time series of hourly air pressure (hPa) along the three colored trajectories shown in (a), from 1200 UTC 16 Jan through 0000 UTC 22 Jan 2010. (c) As in (b), but for water vapor mixing ratio ( $\text{g kg}^{-1}$ ). (d) As in (b), but for relative humidity (%).

for all but the final  $\sim 18$  h, after which synoptic and orographic forcing lifted these parcels (Fig. 10b). During the first three days, these parcels moistened (Fig. 10c) in an offshore region of upward latent-heat fluxes and low-level frontogenesis. Thereafter, mixing ratios decreased during parcel ascent and large relative humidities (Fig. 10d), thus pointing to the removal of water vapor via rainout. All three Arizona-bound trajectories traveled between the high terrain of northern Baja and the Sierra Madre Occidental, thus suggesting a wedge of vulnerability for AR impacts in Arizona, analogous to what was found for the Green River basin in western Washington (Neiman et al. 2011). The trajectory ending at 2 km MSL over Arizona contained more moisture than the cluster of trajectories ending in the core of the AR 12 h earlier, largely because the cluster originated from much higher in the troposphere and experienced long-duration

subsidence. These differing trajectory behaviors over a short period of time highlight the rapidly evolving nature of this strong AR. The evolution of the uppermost trajectory terminating at 3 km MSL more closely matches its earlier counterparts. A more thorough, model-based analysis during the inland penetration phase of the AR will be addressed in Part II of this study.

### 5. Regional hydrometeorological analysis centered on Arizona

This section presents a regional hydrometeorological analysis centered on Arizona during the inland penetration of AR 3. Relevant topographic features include a coastal mountain barrier ( $\sim 1.2\text{--}2.5$  km MSL) in Southern California and Baja, low terrain ( $<0.6$  km MSL) in the Sonoran Desert of southwestern Arizona,

Rawinsonde soundings from Tucson, AZ

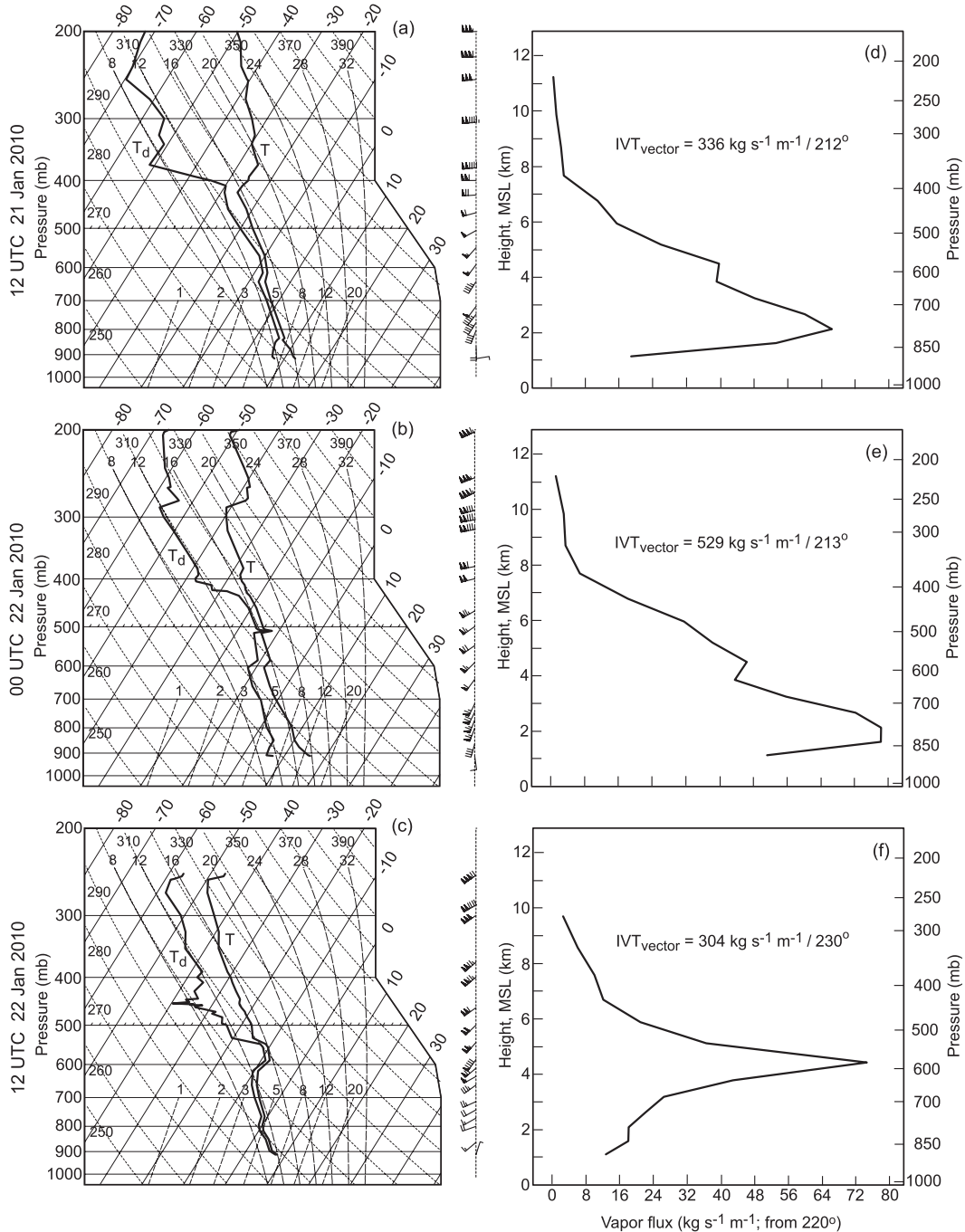


FIG. 11. Skew  $T$ - $\log p$  diagrams of rawinsonde soundings from Tucson, AZ, at (a) 1200 UTC 21 Jan, (b) 0000 UTC 22 Jan, and (c) 1200 UTC 22 Jan 2010. Profiles of temperature ( $T$ ) and dewpoint temperature ( $T_d$ ) are labeled. Wind flags and barbs are as in Fig. 5b. Along-AR water vapor flux profiles ( $\text{kg m}^{-1} \text{s}^{-1}$ ; directed from  $220^\circ$ ) from the same rawinsonde soundings at (d) 1200 UTC 21 Jan, (e) 0000 UTC 22 Jan, and (f) 1200 UTC 22 Jan 2010. The IVT magnitudes and directions between 900 and 300 hPa are shown next to the profiles.

and a high plateau ( $>1400$  m MSL) with protruding mountain ranges ( $>3$  km MSL) across the remainder of the southwestern United States (Fig. 2). Arizona's well-defined, northwest-southeast-oriented

Mogollon Rim rises abruptly from the Sonoran Desert to greater than 2.5 km MSL and represents a formidable orographic obstacle to incoming southwesterly flow.

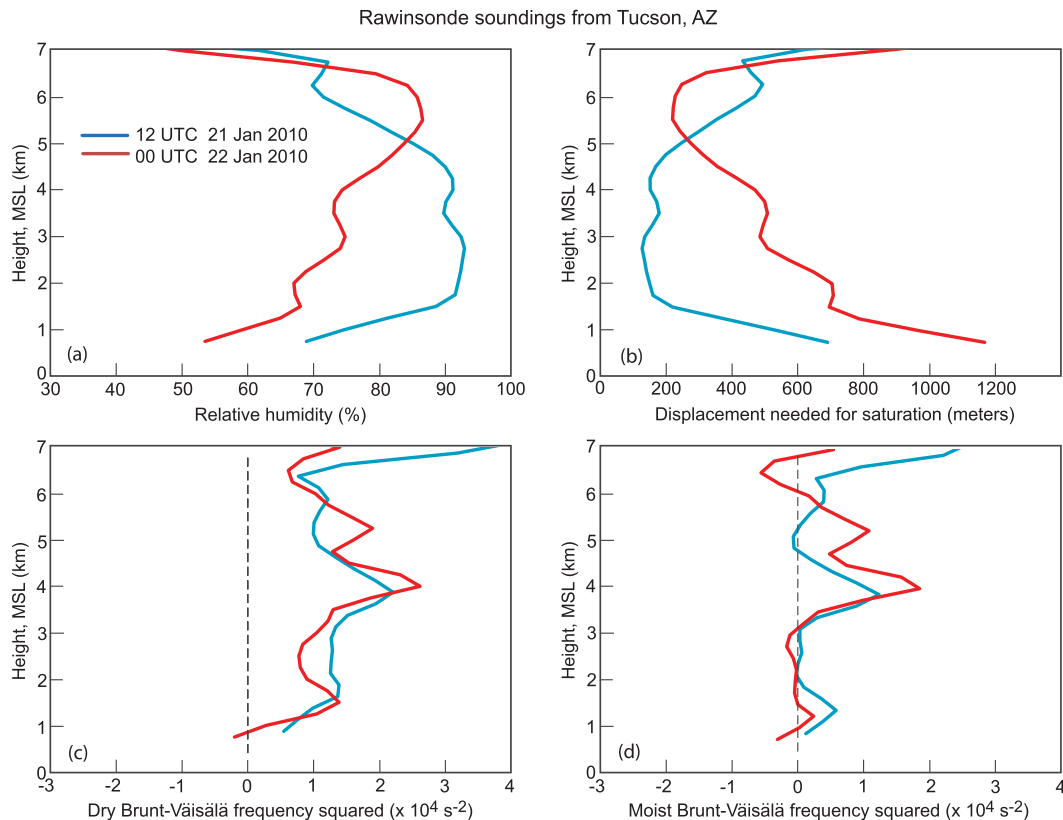


FIG. 12. Profiles from the Tucson, AZ, rawinsonde soundings at 1200 UTC 21 Jan and 0000 UTC 22 Jan 2010 (blue and red, respectively): (a) relative humidity (%); (b) vertical displacement (m) required for saturation; and squares of the (c) dry and (d) moist Brunt-Väisälä frequency ( $10^4 \text{ s}^{-2}$ ; as in Durran and Klemp 1982).

### a. Meteorological characteristics

A sequence of operational rawinsondes launched at Tucson between 1200 UTC 21 and 22 January 2010 provided key observations during and after the passage of the intense AR. Skew  $T$  diagrams (Figs. 11a–c) depict deep-tropospheric moisture and a rising tropopause for the 24-h period. Strengthening low-level southwesterly flow was observed within the AR on 1200 UTC 21 and 0000 UTC 22 January, while, 12 h later, weaker post-AR west-southwesterly flow was situated beneath the polar cold-frontal inversion at 600 hPa. Companion profiles of along-AR horizontal water vapor flux (Figs. 11d–f) show a low-level maximum at  $\sim 2$  km MSL (i.e.,  $\sim 1$  km above the bottom of the lowest flux layer at 900 hPa) which increased in magnitude from 66 to  $78 \text{ kg s}^{-1} \text{ m}^{-1}$  in response to the strengthening low-level southwesterly jet during the approach of the AR. Previous studies of landfalling ARs along the West Coast of the United States (e.g., Ralph et al. 2004, 2005; Neiman et al. 2008b, 2011) show vapor flux maxima  $\sim 1$  km above the ocean surface, thus suggesting a terrain-following character to

ARs. The IVTs in the first two Tucson soundings were directed from  $212^\circ$  to  $213^\circ$  and increased significantly in magnitude (from  $386$  to  $529 \text{ kg s}^{-1} \text{ m}^{-1}$ ), consistent with the CFSR-based plan-view analyses<sup>1</sup> (Figs. 5a, 8a). By 1200 UTC 22 January, the core of the vapor transport in the AR over Tucson ascended to  $\sim 4.5$  km MSL near the leading edge of the temporally ascending polar cold front. The IVT magnitude decreased to  $304 \text{ kg s}^{-1} \text{ m}^{-1}$  and veered to  $230^\circ$  in response to weakening west-southwesterly flow beneath the cold-frontal inversion aloft.

Additional variables from the Tucson rawinsondes are plotted in Fig. 12 for the two earlier times, when strengthening AR conditions and heavy precipitation enveloped the region. Relative humidities (Fig. 12a) exceeded 65%–70% between 1 and 6 km MSL, although

<sup>1</sup> The CFSR dataset is extrapolated downward to sea level over land. Hence, the IVTs measured by the Tucson rawinsondes in the layer between 900 and 300 hPa are overestimated by the 1000–300 hPa IVT from the CFSR.

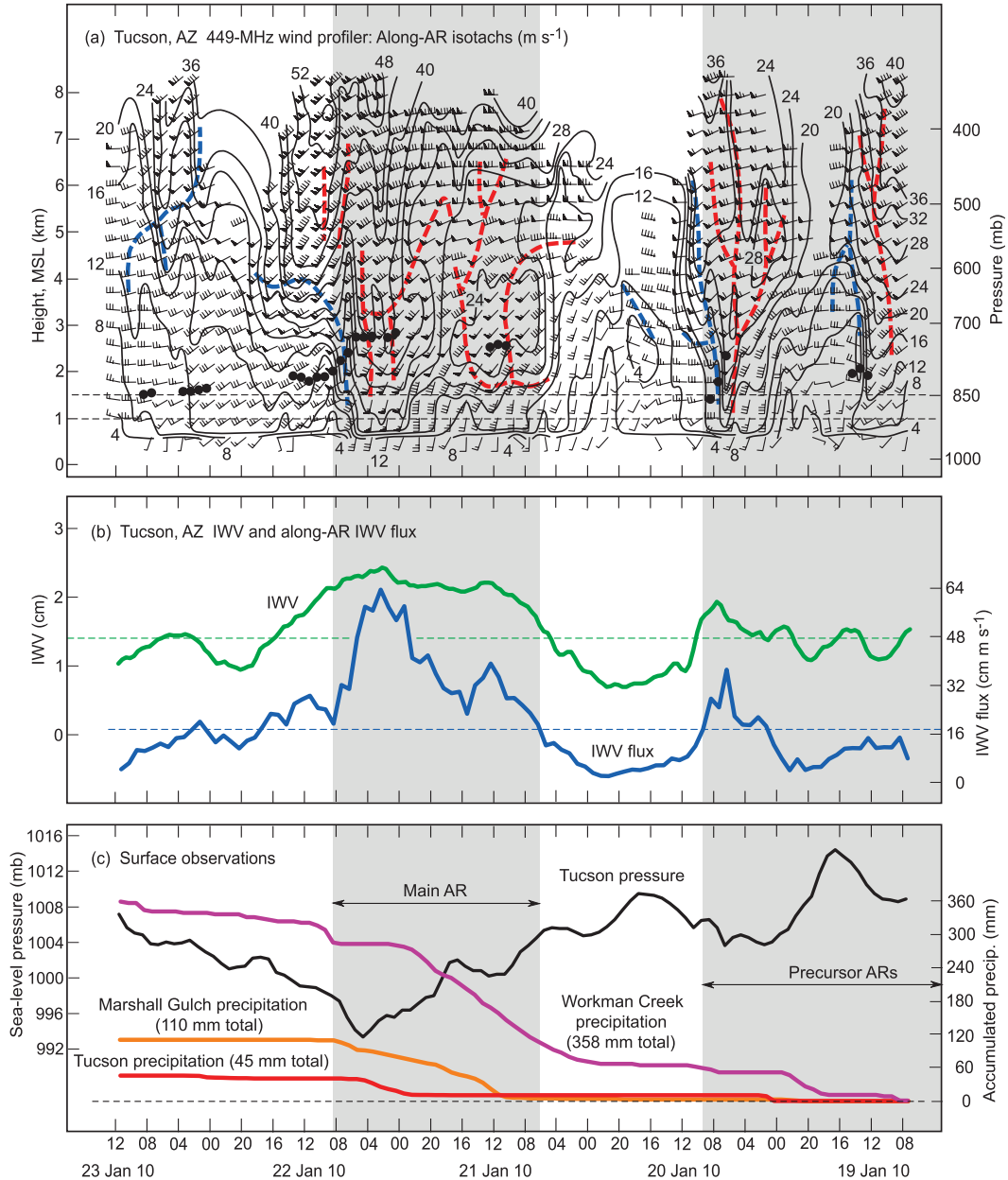


FIG. 13. Time series of observations from south-central Arizona between 0700 UTC 19 Jan and 12 UTC 23 Jan 2010 (time increases from right to left to portray the advection of synoptic features from west to east). (a) Time-height section of hourly averaged wind profiles (flags and barbs are as in Fig. 5b), along-AR isotachs ( $\text{m s}^{-1}$ ; directed from  $220^\circ$ ), brightband melting-level heights (bold black dots), and axes of maximum thermal wind-derived (i.e., geostrophic) warm and cold advection [red and blue dashed lines, respectively; derivation technique described in Neiman and Shapiro (1989)] from the Tucson wind profiler. Every other wind profile and range gate is plotted. The horizontal dashed black lines enclose the layer between 1.0 and 1.5 km MSL where hourly layer-mean along-AR flow (directed from  $220^\circ$ ) and along-AR IWV flux were calculated. (b) Time series of 30-min IWV (cm; green) and hourly, layer-mean, along-AR IWV flux ( $\text{cm m s}^{-1}$ ; blue) from the Tucson wind profiler and nearby GPS receiver. The horizontal dashed green and blue lines mark the AR thresholds for the IWV and IWV flux, respectively (from Ralph et al. 2004; Neiman et al. 2009), adjusted from sea level to the GPS site at 724 m MSL. (c) Time series of sea level pressure (hPa; black) from Tucson and time series of precipitation accumulation (mm) from Tucson (red), Marshall Gulch (orange), and Workman Creek (purple). The gray shaded bars in all three panels mark AR conditions.

COOP and Snotel precipitation analysis  
21–22 January 2010

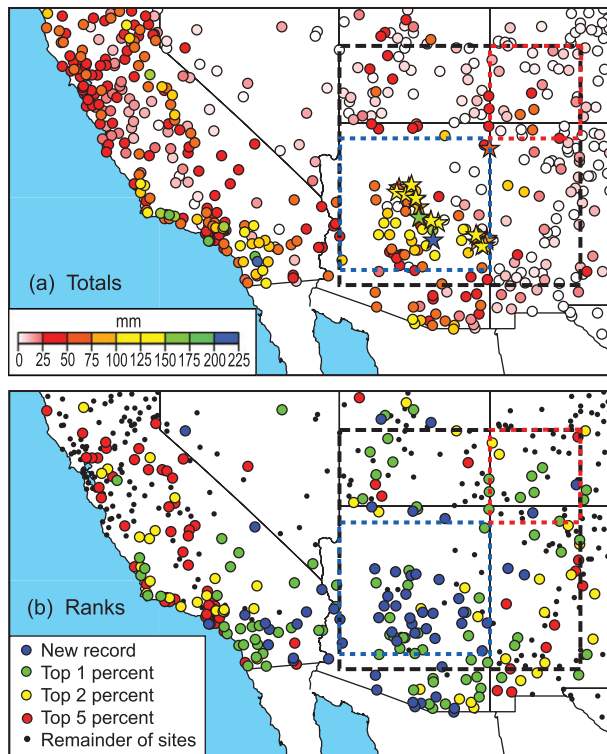


FIG. 14. Daily COOP and Arizona SNOTEL precipitation observations (circles and stars, respectively): (a) 2-day accumulations (mm; color coded, see scale) for 21–22 Jan 2010 and (b) ranking of precipitation accumulation on 21–22 Jan 2010 (percentile; color coded, see scale) relative to all available January pairs of days between 1950 and 2009 for those COOP gauges having recorded data for  $\geq 25$  Januaries. These data are based on local time [add 7 h (8 h) to the Mountain (Pacific) time zone to convert to UTC]. The black, blue, and red boxes show the domains for areal-averaged daily precipitation totals (ending 1200 UTC each day) using the NOAA/Climate Prediction Center's 0.25°-resolution unified precipitation dataset, discussed in the text.

they decreased with time below 5 km MSL between 1200 UTC 21 and 0000 UTC 22 January in response to diurnal heating. Above 1.5 km MSL, vertical air parcel displacements of  $\leq 700$  m were required to reach saturation (Fig. 12b), which is less than the rise of the Mogollon Rim downwind of Tucson and consistent with reports of widespread precipitation and low ceilings across the Mogollon. Profiles of dry and moist Brunt–Väisälä frequency (Figs. 12c,d) reveal weak low-level stability in the airstream approaching the Mogollon Rim. Assuming saturated conditions blanketed the elevated terrain, the strong incoming flow would have encountered no appreciable resistance to orographically forced ascent in the lowest 3 km MSL where moist neutral stratification

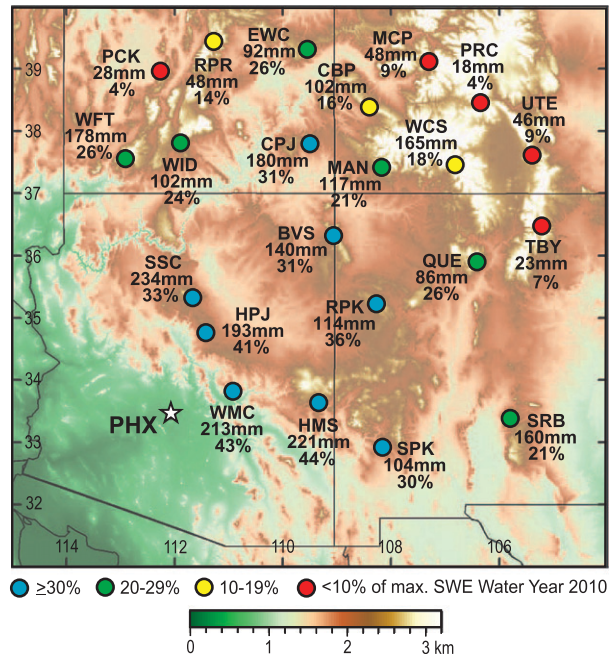


FIG. 15. Terrain base map showing daily data from selected SNOTEL sites for the period 18–23 Jan 2010: absolute magnitude of the 6-day changes in SWE (mm; numerical values only) and 6-day changes as a percentage of maximum SWE for WY2010 (color coded, see scale). The three-letter station names are given. These data are based on local time (add 7 h to convert to UTC). The location of Phoenix (PHX) is marked.

was observed, thus yielding efficient and heavy orographic precipitation. Similar conditions have been found in landfalling ARs along the U.S. West Coast, from California to Washington (e.g., Ralph et al. 2005; Neiman et al. 2008b, 2011).

The wind profiler and GPS receiver near Tucson provided a detailed account of the tropospheric winds and IWV (Figs. 13a,b). The two precursor AR events on 19–20 January (i.e., ARs 1 and 2) were accompanied by enhanced southwesterly flow, a modest increase in IWV and along-AR IWV flux,<sup>2</sup> and geostrophic warm advection, followed by a wind shift to westerly flow, a decrease in IWV and IWV flux, and geostrophic cold advection. The radar melting level was situated at  $\sim 1.8$  km MSL during AR 1 and descended from 2.2 to 1.4 km MSL in the cold advection behind AR 2.

<sup>2</sup> The along-AR IWV flux is defined as the product of the along-AR component of the flow (from 220°) measured hourly by the Tucson wind profiler in the layer between 1.0 and 1.5 km MSL and the hourly IWV measured at the nearby GPS receiver. A variant of this technique is described in Neiman et al. (2009). Because water vapor is typically concentrated in the lower troposphere, the IWV flux is a first-order estimate of low-level water vapor flux.

TABLE 1. A list of selected SNOTEL sites, locations, elevations, 6-day changes in SWE from 18 through 23 Jan 2010, 6-day changes in SWE as a percent of maximum SWE for WY2010, and maximum SWE for WY2010.

Site	Three-letter name	State	Lat (°N)	Lon (°W)	Altitude (m)	$\Delta$ SWE (mm)	$\Delta$ SWE as %	Max SWE (mm)
						1200 UTC 18–23 Jan 2010	of max SWE WY2010	WY2010
Snowslide Canyon	SSC	AZ	35.33	111.65	2966	234	33	704
Happy Jack	HPJ	AZ	34.75	111.42	2326	193	41	470
Workman Creek	WMC	AZ	33.82	110.92	2103	213	43	493
Hannagan Meadows	HMS	AZ	33.65	109.32	2749	221	44	508
Beaver Spring	BVS	AZ	36.33	109.05	2804	140	31	445
Rice Park	RPK	NM	35.23	108.27	2579	114	36	318
Signal Peak	SPK	NM	32.92	108.15	2548	104	30	348
Quezamon	QUE	NM	35.92	106.40	2896	86	26	330
Sierra Blanca	SRB	NM	33.40	105.78	3133	160	21	747
Tolby	TBY	NM	36.47	105.20	3103	23	7	343
Webster Flat	WFT	UT	37.57	112.90	2795	178	26	688
Pine Creek	PCK	UT	38.97	112.25	2679	28	4	632
Widtsoe	WID	UT	37.83	111.88	2983	102	24	427
Red Pine Ridge	RPR	UT	39.45	111.27	2746	48	14	348
East Willow Creek	EWC	UT	39.32	109.53	2530	91	26	345
Camp Jackson	CPJ	UT	37.82	109.48	2733	180	31	584
Columbine Pass	CBP	CO	38.42	108.38	2865	102	16	635
Mancos	MAN	CO	37.43	108.17	3048	117	21	556
McClure Pass	MCP	CO	39.13	107.28	2896	48	9	516
Wolf Creek Summit	WCS	CO	37.48	106.80	3353	165	18	942
Porphyry Creek	PRC	CO	38.48	106.33	3280	18	4	424
Ute Creek	UTE	CO	37.62	105.37	3246	46	9	493

During these ARs,  $\sim 60$  mm of precipitation fell at the high-elevation Workman Creek SNOTEL site along the south flank of the Mogollon Rim (2103 m MSL; Fig. 2), while much less precipitation fell in Tucson and in the nearby mountains at Marshall Gulch (2290 m MSL). Thereafter, an extended period of dry IWVs ( $<1.4$  cm), weak IWV fluxes ( $<17.5$  cm  $s^{-1}$ ), and little precipitation occurred between 0900 UTC 20 January and 0600 UTC 21 January prior to the onset of the intense AR 3. During this quiescent period, low-level westerly flow eventually backed to southerly in response to the passage of a transient shortwave ridge (cf. the accompanying Tucson pressure trace in Fig. 13c) ahead of AR 3.

The 26 h between 0600 UTC 21 January and 0800 UTC 22 January 2010 marked the period of intense AR conditions when enhanced water vapor and strong low-level southwesterly flow combined to produce large IWV and strong terrain-normal IWV fluxes that exceeded AR thresholds at the inland site in Tucson (1.4 cm and 17.5 cm  $m s^{-1}$ , respectively) (Fig. 13). These thresholds are 30% smaller than those used along the U.S. West Coast at sea level (Ralph et al. 2004; Neiman et al. 2009) because the Tucson GPS site is situated at 724 m MSL and contains correspondingly less IWV, on average, than at sea level. The period of strong orographic forcing coincided with weak moist static stability (Figs. 12c,d)

and occurred in conjunction with deep geostrophic warm advection and synoptic-scale ascent (section 4b). High melting levels (2.5–2.8 km MSL) accompanied the AR, as is common in ARs along the U.S. West Coast (e.g., Neiman et al. 2008a, 2011; Ralph et al. 2011). Following the passage of a pressure trough, the IWV flux and melting level decreased between 0500 and 0900 UTC 22 January in response to a cold-frontal wind shift (from strong south-southwesterly to weaker southwesterly) and geostrophic cold advection below  $\sim 4$  km MSL. Above this transition, strong pre-cold-frontal southwesterly flow ( $>40$  m  $s^{-1}$ ) persisted until 1400 UTC 22 January, and the enhanced water vapor in this layer aloft (Fig. 11c) contributed to a slower decline in IWV than IWV flux. For the 26-h period of intense AR conditions, 206 mm of precipitation fell at Workman Creek on the Mogollon.

#### b. Hydrometeorological analysis

The intense AR severely impacted Arizona on 21–22 January, owing to its anomalous strength and weak low-level static stability. Upon landfall, the intense AR generated significant 2-day COOP- and SNOTEL-observed precipitation totals across California (Fig. 14a), with the greatest accumulations ( $>100$  mm) occurring in the steep coastal mountain ranges in the south. Farther east, Arizona received widespread precipitation, including

(a) Rank among all January pairs of days (1901-2009) of streamflow on 21-22 Jan 2010. USGS streamflow gages on unregulated channels with >25 Januarys of record.

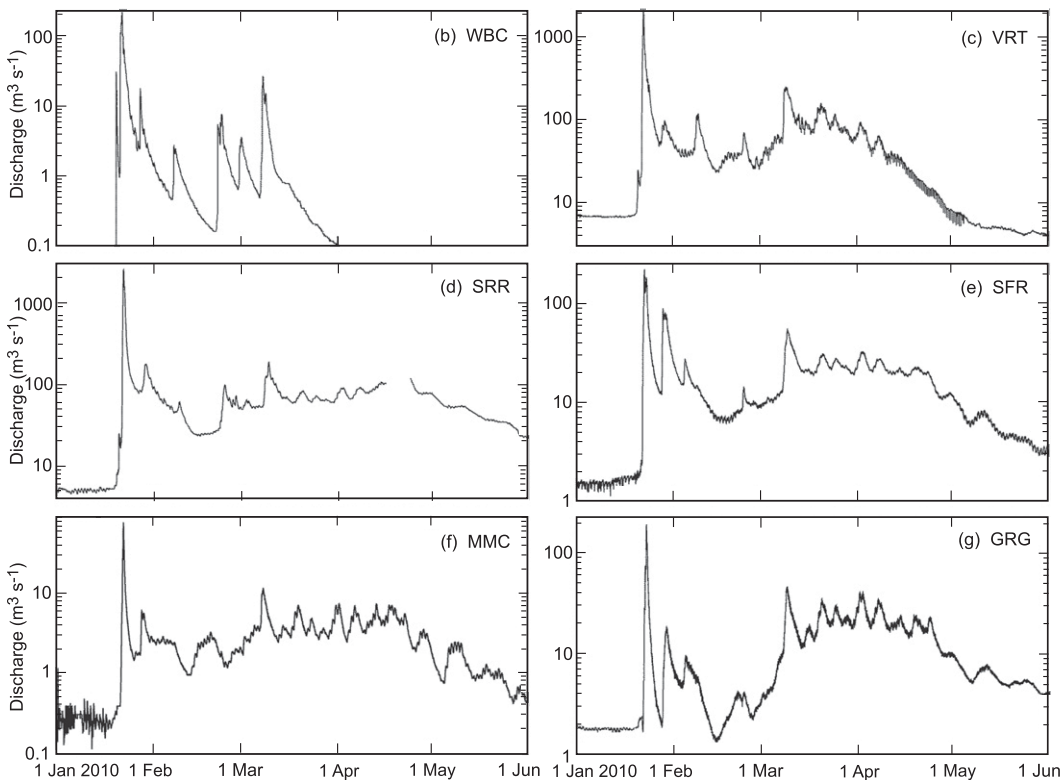
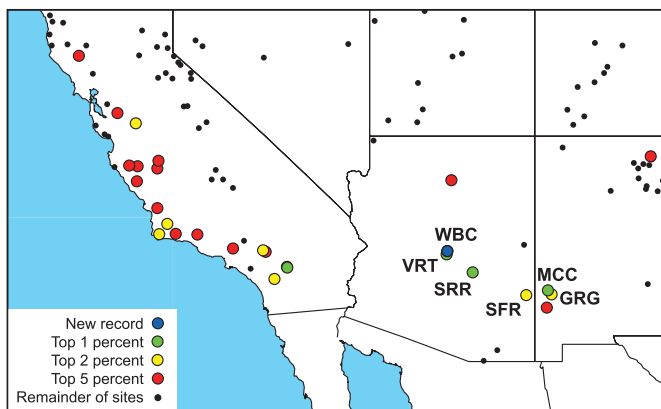


FIG. 16. (a) Ranking of daily (local time) unregulated streamflows on 21-22 Jan 2010 (percentile; color-coded, see scale) relative to all available January pairs of days (1901 and 2009) for those gauges having recorded data for  $\geq 25$  Januarys. Time series of  $\sim 15$ -min-resolution streamflow ( $\text{m}^3 \text{s}^{-1}$ ; log scale, except at WBC, where the base flow was 0) for the period 1 Jan to 1 Jun 2010 at (b) WBC, (c) VRT, (d) SRR, (e) SFR, (f) MCC, and (g) GRG. (See Table 2 for full location names.)

a broad region of heavy accumulations ( $>100$  mm) in the vicinity of the Mogollon Rim. Lesser, but still significant, precipitation fell across the neighboring states. A ranked precipitation analysis based on gauge sites that collected data for at least 25 of the last 50 Januarys (Fig. 14b) shows the greatest number of record 2-day accumulations over Arizona, plus many near-record totals

region-wide. To further quantify these results, the CPC's gridded UPD was used to calculate and rank areal-averaged daily precipitation values across three domains between 1970 and 2010: the southwestern United States, Arizona, and southwest Colorado (black, blue, and red boxes in Fig. 14). The areal averages were computed at 1200 UTC of each day by dividing the sum of all daily

TABLE 2. A list of selected USGS stream gauge sites, locations, elevations, basin areas, ~15-min-resolution magnitudes with date and time of maximum flow for the AR of 21–22 Jan. 2010, and the rank (percentile) among all January pairs of days (1901–2009) of streamflow on 21–22 Jan 2010. The listed gauges are on unregulated channels with  $\geq 25$  Januarys of record.

Site	Three-letter name	State	Lat (°N)	Lon (°W)	Gauge altitude (m)	Basin area (km <sup>2</sup> )	Years of record (yr)	Max flow (m <sup>3</sup> s <sup>-1</sup> )	Time of max flow in 2010	Actual percentile	Symbol on base map
Wet Bottom Creek, near Childs	WBC	AZ	34.16	111.69	707	94	43	207	0545 UTC 22 Jan	0%	Record
Verde River, below Tangle Creek	VRT	AZ	34.07	111.72	618	14 224	25	2046	0915 UTC 22 Jan	0.50%	1%
Salt River, near Roosevelt	SRR	AZ	33.62	110.92	664	11 148	97	2499	1030 UTC 22 Jan	0.50%	1%
San Francisco River, at Clifton	SFR	AZ	33.05	109.30	1047	7153	97	218	1815 UTC 22 Jan	1.80%	2%
Mogollon Creek, near Cliff	MCC	NM	33.17	108.65	1658	179	43	77	1230 UTC 22 Jan	0.50%	1%
Gila River, near Gila	GRG	NM	33.06	108.54	1419	4826	82	191	0045 UTC 23 Jan	1.30%	2%

precipitation values on the 0.25° grid within each domain by the number of grid cells in that domain. They were then ranked. For the southwestern United States and Arizona domains, the largest daily totals in 40 years (19.25 and 35.56 mm, respectively) fell on 21 January. These top-ranked values exceeded the fifth-ranked values by 58% and 79%, respectively, further highlighting the extreme nature of this event, especially across Arizona. Southwest Colorado attained a rank of 22 on 21 January, thus pointing to lessening hydrometeorological impacts as the AR penetrated further inland.

Figure 15 and Table 1 highlight changes in SWE at selected SNOTEL sites across the southwestern United States during the 6-day period of active weather between 18 and 23 January. All sites show increases due to snow accumulation and/or absorption of rain by the existing snowpack, and these increases occurred primarily during the intense AR between 20 and 22 January. The largest gains in SWE were focused in Arizona (140–234 mm), with lesser but still noteworthy gains occurring in the neighboring states of Utah (28–180 mm), New Mexico (23–160 mm), and Colorado (18–165 mm). To place these results into seasonal hydrological context, the SWE observations are also expressed as a percentage of the maximum SWE during water year 2010 (WY2010; which was abnormally snowy across the desert Southwest). In Arizona, the 6-day gains represented 31%–44% of the maximum SWE. The percentages generally decreased with increasing distance from Arizona, thus revealing a lessening influence of the AR deeper into the interior of the continent. Near Colorado’s San Juan Mountains, large increases in SWE (i.e., >100 mm) represented only moderate percentages of the water-year maximum because the San Juans typically receive substantial seasonal snowfall. The water-year percentage at East Willow Creek, Utah (EWC; 26%), was much larger than neighboring sites and suggests the importance of water vapor channeling up the Colorado River basin. The SWE results presented here for the interior southwestern United States mirror those described in Neiman et al. (2008b) and Guan et al. (2012), which show significant contributions to the snowpack in California’s Sierra Nevada by landfalling ARs.

In response to the heavy precipitation and high melting levels, and given that the two earlier ARs moistened the soil, near-record 2-day runoff occurred from the coastal mountains of Southern California to Arizona to southwest New Mexico (Fig. 16a). The ranked analysis in Fig. 16a requires at least 25 Januarys of daily records at gauges residing downstream of unregulated channels. Despite the fact that Arizona has comparatively few such gauges, the flooding signal is still apparent, with Wet Bottom Creek (WBC) receiving the January flood

of record and Verde River (VRT) and Salt River (SRR) experiencing January floods in the top 1%. Six key gauges that received high-rank floods (see station names in Fig. 16a) range in altitude from 618 to 1658 m MSL, and the basin areas above these sites vary by more than two orders of magnitude, from 94 to 14 224 km<sup>2</sup> (Table 2). In contrast, the maximum flows spanned only approximately one order of magnitude, from 207 m<sup>3</sup> s<sup>-1</sup> in the small basin at WBC to 2499 m<sup>3</sup> s<sup>-1</sup> in the much larger basin at SRR, because the larger basins extend to high elevations where snow fell during part of the storm and/or rain was absorbed by the existing substantial snowpack. The local hydrogeology may have also played a role in these differences, although, generally, the entire Mogollon Rim region is characterized by low-permeability bedrock with relatively thin soils (Stonstrom et al. 2007), factors that tend to enhance rapid runoff from storms. The AR-influenced spike in flow at these six gauges is readily apparent in Figs. 16b–g and represents the largest daily flows for water year 2010. Following the spike, a broad springtime period of enhanced snowmelt-induced flows was observed, except at the small, low-elevation gauge at WBC. The physical processes associated with flooding during this inland-penetrating AR event also typically contribute to flooding during the landfall of ARs in the mountainous terrain along the west coasts of the United States and the United Kingdom (e.g., Dettinger 2004; Ralph et al. 2006, 2011; Dettinger et al. 2011; Lavers et al. 2011; Neiman et al. 2011).

The catchment basin above the SRR gauge (Fig. 17) is representative of other large basins draining the south side of the Mogollon Rim. Significantly, nearly three-quarters of the catchment above SRR is a broad plateau between 1.5 and 2.5 km MSL. This hydrologically sensitive altitude band is situated well below the unusually high melting levels (2.5–2.8 km MSL) observed by the Tucson wind profiler during the intense AR on 21–22 January (Fig. 13a), such that 90%–98% of the catchment basin received heavy rain rather than snow. The temporal phasing of very high melting levels with the heavy precipitation in this AR quite likely led to the major region-wide flooding (e.g., White et al. 2002; Lundquist et al. 2008), similar to what has been observed with AR landfalls along the U.S. West Coast (e.g., Neiman et al. 2008a, 2011; Dettinger et al. 2009). Rain-induced snowmelt can secondarily contribute to runoff during warm storms with high melting levels (e.g., McCabe et al. 2007).

## 6. Conclusions

In late January 2010, a series of transient baroclinic waves impacted the southwestern United States. The

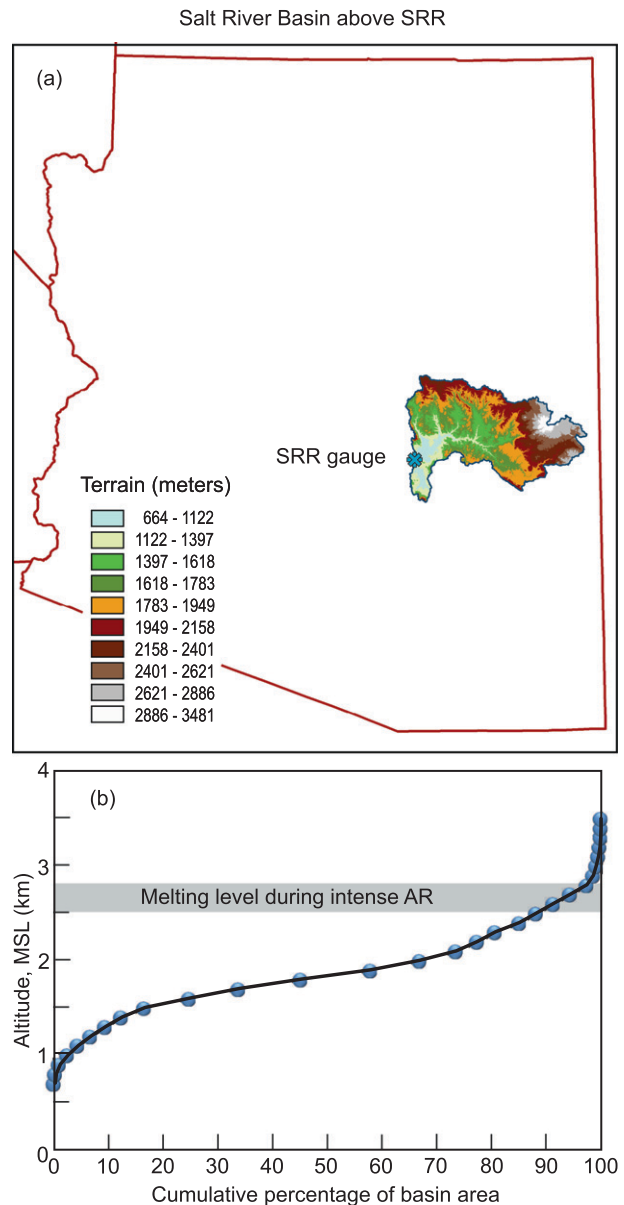


FIG. 17. (a) Color rendering of the terrain altitude in Arizona's Salt River basin (see color scale) above the SRR stream gauge, and (b) cumulative percentage of basin area as a function of basin elevation upstream of the SRR gauge. These analyses were generated using the 30-m horizontal resolution USGS National Elevation Dataset. The gray shaded bar marks the melting-level altitude range recorded by the Tucson wind profiler during the AR of 21–22 Jan 2010.

leading disturbances produced significant precipitation across Arizona that moistened the watersheds. The last of these storms, on 21–22 January, was accompanied by an intense AR that caused record-setting precipitation and flooding across the state. This study confirms the hypothesis that AR conditions can penetrate inland from the Pacific Ocean to central Arizona and produce

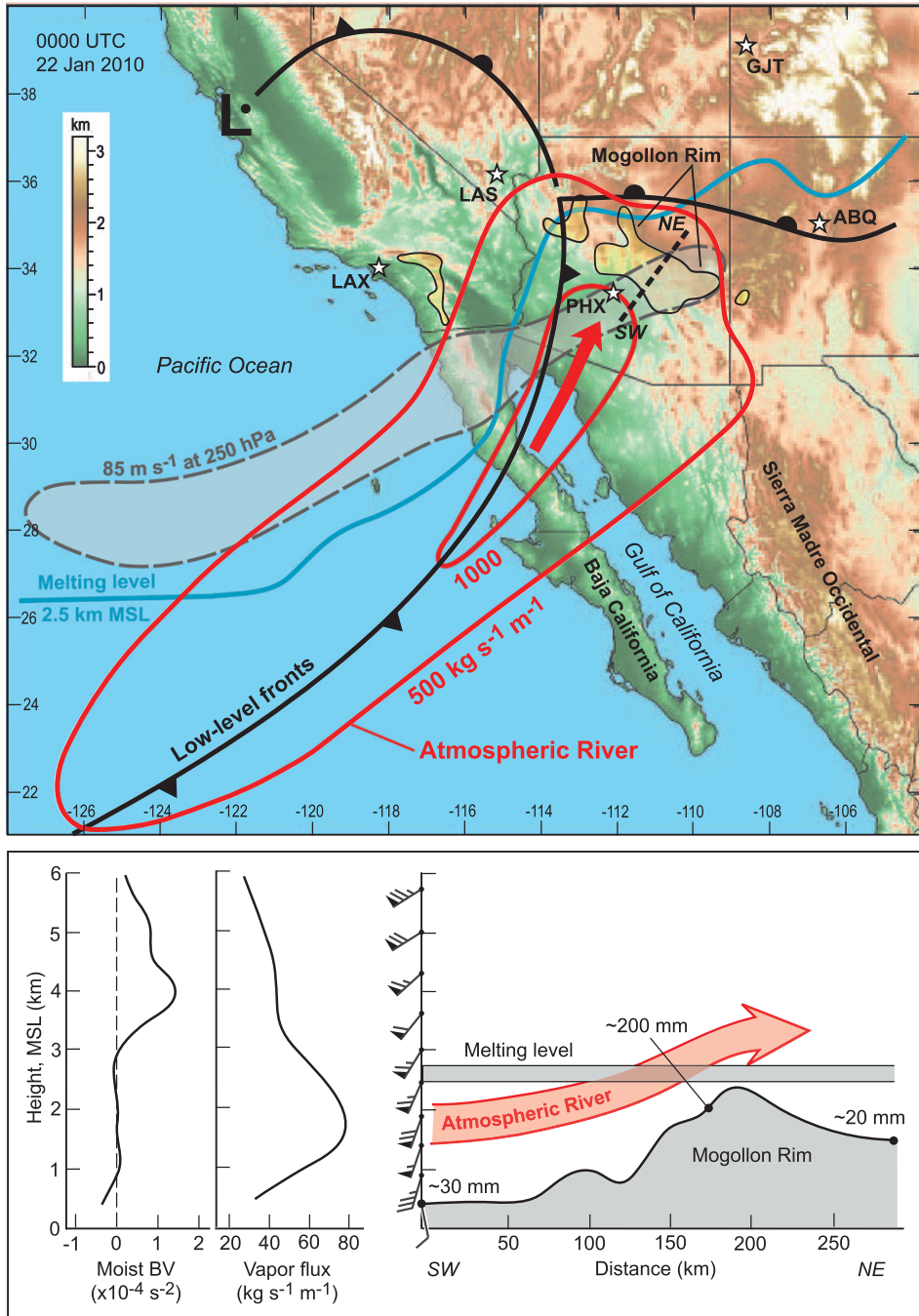


FIG. 18. Conceptual representation of the atmosphere at 0000 UTC 22 Jan and 24-h precipitation accumulations ending at 1200 UTC 22 Jan 2010. (top) Plan-view schematic of IVT magnitude (red contours, with units of  $\text{kg s}^{-1} \text{m}^{-1}$ ; bold red arrow shows the IVT vector direction in the AR core), the  $85 \text{ m s}^{-1}$  isotach (gray dashed contour; interior shading  $>85 \text{ m s}^{-1}$ ), the melting level at 2.5 km MSL (blue contour; estimated from the CFSR  $0^\circ\text{C}$  altitude at 2.7 km, with the assumption that the melting level is located  $\sim 200 \text{ m}$  below the  $0^\circ\text{C}$  isotherm) (e.g., Stewart et al. 1984; White et al. 2002), and the 75-mm isohyets (thin solid contours; interior yellow shading  $>75 \text{ mm}$ ). The black dashed line along SW-NE shows the baseline for the cross section in the bottom panel. Standard notation is used for the near-surface fronts. Cities and terrain are as in Fig. 2. (bottom) Cross-section schematic across the Mogollon Rim (along SW-NE in the top panel) showing the melting level (gray shaded bar), the atmospheric river (red arrow), and representative 24-h precipitation totals (mm) at three locations (bold black dots). The following vertical profiles at the southwest end of the cross section are also shown: wind velocity (flags and barbs are as in Fig. 5b), water vapor flux ( $\text{kg s}^{-1} \text{m}^{-1}$ ; directed from  $220^\circ$ ), and moist Brunt-Väisälä frequency squared ( $10^4 \text{ s}^{-2}$ ).

extreme hydrometeorological impacts there. Key factors that led to these impacts are discussed below and illustrated in a conceptual schematic (Fig. 18).

SSMIS satellite imagery and CFSR gridded analyses of the storm of 21–22 January show collocated, long and narrow pre-cold-frontal plumes of enhanced IWV and IVT that met the criteria used to define AR conditions. Dynamical forcing associated with an upper-level jet and associated PV anomaly created a strong cyclogenetic response at low levels, which contributed to low-level frontogenesis and enhanced sea surface latent-heat fluxes that concentrated the water vapor and its transport into its narrow, filamented structure offshore. The AR then came ashore across Baja and into Arizona. Back-trajectory analyses revealed that the collocated IWV and IVT plumes within the intense AR of 21–22 January strengthened markedly and rapidly during landfall via extratropical dynamical processes without entraining tropical water vapor.

Regional observing platforms across central Arizona, including a fortuitously deployed wind profiler and GPS receiver, recorded strong, moist northeastward-directed flow and moist neutral stratification in the lowest 3 km of the atmosphere. The moist neutrality in this case matches the mean observed characteristics from 17 dropsondes released into ARs over the Pacific (Ralph et al. 2005). Similarly, most of the water vapor transport was concentrated in the lower troposphere. Given the presence of weak static stability, strong incoming water vapor fluxes oriented perpendicular to the northwest–southeast escarpment of the Mogollon Rim, and large-scale dynamics, orographically enhanced heavy precipitation was focused in the center of the state and lasted for more than 24 h. It is reasonable to surmise that the intense character of the incoming vapor fluxes was partly a consequence of the precise positioning of the AR across the relatively low mountains of southern Baja south of 30°N (rather than across the much higher, northern portion of this range) and west of Mexico's Sierra Madre Occidental, because only a fraction of the water vapor within the AR over the eastern Pacific was likely lost to orographic processes upwind of Arizona. During the persistent heavy precipitation over central Arizona, unusually high melting levels in the AR environment resulted in rain (rather than snow) falling at high elevations over much larger catchment areas than during a typical storm, thus leading to greatly enhanced runoff volumes and flooding. Additional factors contributing to the runoff included snowmelt from the anomalously large snowpack, previously saturated soils, and relatively impermeable bedrock with overlying thin soils.

Overall, the characteristics of the intense, landfalling AR of 21–22 January 2010, and the resulting heavy

orographic precipitation and flooding in Arizona, are comparable to those of landfalling ARs and their impacts along the west coasts of midlatitude continents elsewhere (e.g., Dettinger 2004; Ralph et al. 2006, 2011; Stohl et al. 2008; Reeves et al. 2008; Neiman et al. 2008a,b, 2009, 2011; Smith et al. 2010; Viale and Nuñez 2011; Dettinger et al. 2011; Lavers et al. 2011; Guan et al. 2012; Ralph and Dettinger 2012). Thus, findings regarding implications of strong ARs striking coastal areas are relevant farther inland, including an extreme event that caused damage to a key flood control reservoir near Seattle, Washington (White et al. 2012), and risks of a catastrophe in California quantified through the “ARkStorm” emergency preparedness scenario (Dettinger et al. 2012). The present case study, combined with the recent study by Rutz and Steenburgh (2012) showing substantial contributions of annual precipitation in Arizona following the landfall of ARs across Baja, highlight the fact that large storms, floods, and water supplies of Arizona are strongly affected by cool-season ARs. Thus, management of Arizona's flood risks and water supplies may benefit from advancing our understanding, monitoring, and forecasting of inland-penetrating ARs. Future research on this case will utilize high-resolution simulations to investigate water vapor pathways directed from the Pacific coast into the interior. For Arizona, ARs must bypass a single, nearly continuous high range in Southern California and northern Baja. In contrast, farther north, decidedly more convoluted pathways are likely required to bring AR moisture across the complex and landlocked topography there, such as occurred during a flood in Montana's Glacier National Park in November 2006 (Bernhardt 2006; Neiman et al. 2008a).

Because water is a critically limited resource in Arizona, which is home to Phoenix, the nation's sixth-largest city, it is important to understand what types of weather systems most effectively bring precipitation to the region and how the frequency and intensity of those systems might change in a warming climate (with the acknowledgment that much of the state's water comes from the Colorado River far upstream). Dettinger et al. (2011) showed that most of Arizona receives half of its annual precipitation in  $\leq 15$  days. These wet days occur mostly with winter storms (often ARs) and during the summer monsoon (M. D. Dettinger 2012, personal communication). Arizona is presently near the southern end of the wintertime midlatitude storm track. In a changing climate where the winter storm track is likely to move northward (e.g., Yin 2005), it is imperative to understand if and how a semiarid interior region like Arizona might lose a substantial fraction of its annual precipitation and if the terrain upwind will exacerbate the

problem of bringing the remaining water vapor inland for rainout. The first results of climate change impacts on AR conditions were presented by Dettinger (2011), which showed the potential for rare but more extreme AR events striking neighboring California.

*Acknowledgments.* This project was funded in part by Cooperative Agreement R11AC81334 between the Bureau of Reclamation and the Cooperative Institute for Research in Environmental Sciences at the University of Colorado. Jim Adams assisted in the electronic drafting of figures. Allen White generated the terrain base maps. Darren Jackson provided customized satellite imagery. Chengmin Hsu of NOAA-CIRES created the graphics showing the cumulative fraction of basin area for Arizona's Salt River. We appreciate the comments and suggestions by Michael Alexander and Kevin Werner of NOAA and from three anonymous reviewers. Their efforts improved the scope and quality of this manuscript.

#### REFERENCES

- Beebe, R. G., and F. C. Bates, 1955: A mechanism for assisting in the release of convective instability. *Mon. Wea. Rev.*, **83**, 1–10.
- Bernhardt, D., 2006: Glacier National Park Flooding November 2006. NWS Western Region Tech. Attachment 08-23, 15 pp. [Available online at [http://www.wrh.noaa.gov/media/wrh/online\\_publications/talite/talite0823.pdf](http://www.wrh.noaa.gov/media/wrh/online_publications/talite/talite0823.pdf).]
- Browning, K. A., 1990: Organization of clouds and precipitation in extratropical cyclones. *Extratropical Cyclones: The Erik Palmén Memorial Volume*, C. W. Newton and E. Holopainen, Eds., Amer. Meteor. Soc., 129–153.
- Calloway, C. G., 2003: *One Vast Winter Count—The Native American West before Lewis and Clark*. University of Nebraska Press, 631 pp.
- Carlson, T. N., 1991: *Mid-Latitude Weather Systems*. Harper-Collins, 507 pp.
- Dettinger, M. D., 2004: Fifty-two years of “pineapple-express” storms across the west coast of North America. California Energy Commission Rep. CEC-500-2005-004, 15 pp. [Available online at <http://www.energy.ca.gov/2005publications/CEC-500-2005-004/CEC-500-2005-004.PDF>.]
- , 2011: Climate change, atmospheric rivers, and floods in California—A multimodel analysis of storm frequency and magnitude changes. *J. Amer. Water Resour. Assoc.*, **47**, 514–523, doi:10.1111/j.1752-1688.2011.00546.x.
- , H. Hidalgo, T. Das, D. Cayan, and N. Knowles, 2009: Projection of potential flood regime changes in California. California Energy Commission Rep. CEC-500-2009-050-D, 68 p.
- , F. M. Ralph, T. Das, P. J. Neiman, and D. Cayan, 2011: Atmospheric rivers, floods, and the water resources of California. *Water*, **3**, 455–478.
- , and Coauthors, 2012: Design and quantification of an extreme winter storm scenario for emergency preparedness and planning exercises in California. *Nat. Hazards*, **60**, 1085–1111.
- Draxler, R. R., and G. D. Hess, 1997: Description of the HYSPLIT\_4 modeling system. NOAA Tech. Memo. ERL ARL-224, NOAA/Air Resources Laboratory, Silver Spring, MD, 24 pp.
- , and G. D. Rolph, cited 2011: HYSPLIT (HYbrid Single-Particle Lagrangian Integrated Trajectory) model. NOAA/Air Resources Laboratory. [Available online at <http://ready.arl.noaa.gov/HYSPLIT.php>.]
- Duan, J. M., and Coauthors, 1996: GPS meteorology: Direct estimation of the absolute value of precipitable water. *J. Appl. Meteor.*, **35**, 830–838.
- Durrán, D. R., and J. B. Klemp, 1982: On the effects of moisture on the Brunt–Vaisala frequency. *J. Atmos. Sci.*, **39**, 2152–2158.
- Guan, B., D. E. Waliser, N. P. Molotch, E. J. Fetzer, and P. J. Neiman, 2012: Does the Madden–Julian oscillation influence wintertime atmospheric rivers and snowpack in the Sierra Nevada? *Mon. Wea. Rev.*, **140**, 325–342.
- Hart, R. E., and R. H. Grumm, 2001: Using normalized climatological anomalies to rank synoptic-scale events objectively. *Mon. Wea. Rev.*, **129**, 2426–2442.
- Higgins, R. W., V. B. S. Silvia, W. Shi, and J. Larson, 2007: Relationships between climate variability and fluctuations in daily precipitation over the United States. *J. Climate*, **20**, 3561–3579.
- Lavers, D. A., R. P. Allan, E. F. Wood, G. Villarini, D. J. Brayshaw, and A. J. Wade, 2011: Winter floods in Britain are connected with atmospheric rivers. *Geophys. Res. Lett.*, **38**, L23803, doi:10.1029/2011GL049783.
- Leung, L. R., and Y. Qian, 2009: Atmospheric rivers induced heavy precipitation and flooding in the western U.S. simulated by the WRF regional climate model. *Geophys. Res. Lett.*, **36**, L03820, doi:10.1029/2008GL036445.
- Lundquist, J. D., P. J. Neiman, B. E. Martner, A. B. White, D. J. Gattas, and F. M. Ralph, 2008: Rain versus snow in the Sierra Nevada, California: Comparing Doppler profiling radar and surface observations of melting level. *J. Hydrometeorol.*, **9**, 194–211.
- Mattioli, V., E. R. Westwater, C. Cimini, J. S. Liljegren, B. M. Lesht, S. I. Gutman, and F. J. Schmidlin, 2007: Analysis of radiosonde and ground-based remotely sensed PWV data from the 2004 North Slope of Alaska Arctic Winter Radiometric Experiment. *J. Atmos. Oceanic Technol.*, **24**, 415–431.
- McCabe, G. J., M. P. Clark, and L. E. Hay, 2007: Rain-on-snow events in the western United States. *Bull. Amer. Meteor. Soc.*, **88**, 319–328.
- Neiman, P. J., and M. A. Shapiro, 1989: Retrieving horizontal temperature gradients and advective flows from single-station wind profiler observations. *Wea. Forecasting*, **4**, 222–233.
- , F. M. Ralph, G. A. Wick, Y.-H. Kuo, T.-K. Wee, Z. Ma, G. H. Taylor, and M. D. Dettinger, 2008a: Diagnosis of an intense atmospheric river impacting the Pacific Northwest: Storm summary and offshore vertical structure observed with COSMIC satellite retrievals. *Mon. Wea. Rev.*, **136**, 4398–4420.
- , —, —, J. Lundquist, and M. D. Dettinger, 2008b: Meteorological characteristics and overland precipitation impacts of atmospheric rivers affecting the West Coast of North America based on eight years of SSM/I satellite observations. *J. Hydrometeorol.*, **9**, 22–47.
- , A. B. White, F. M. Ralph, D. J. Gattas, and S. I. Gutman, 2009: A water vapour flux tool for precipitation forecasting. *Water Manage.*, **162**, 83–94.
- , L. J. Schick, F. M. Ralph, M. Hughes, and G. A. Wick, 2011: Flooding in western Washington: The connection to atmospheric rivers. *J. Hydrometeorol.*, **12**, 1337–1358.
- Newman, M., G. N. Kiladis, K. M. Weickmann, F. M. Ralph, and P. D. Sardeshmukh, 2012: Relative contributions of synoptic and low-frequency eddies to time-mean atmospheric moisture transport, including the role of atmospheric rivers. *J. Climate*, **25**, 7341–7361.

- NOAA, 2007: Coastal wind profiler technology evaluation: An integrated ocean system project. Final Rep. to the IOOS Program Office in the National Ocean Service, 57 pp. [Available online at [http://www.esrl.noaa.gov/psd/psd2/programs/ioos/pdf/IOOS\\_Final%20Report\\_Nov\\_15\\_2007.pdf](http://www.esrl.noaa.gov/psd/psd2/programs/ioos/pdf/IOOS_Final%20Report_Nov_15_2007.pdf).]
- NCDC, 2010: *Storm Data*. Vol. 52, No. 1, 250 pp.
- Petterssen, S., 1956: *Motion and Motion Systems*. Vol. 1. *Weather Analysis and Forecasting*, 2nd ed. McGraw-Hill, 428 pp.
- Ralph, F. M., and M. D. Dettinger, 2012: Historical and national perspectives on extreme west coast precipitation associated with atmospheric rivers during December 2010. *Bull. Amer. Meteor. Soc.*, **93**, 783–790.
- , P. J. Neiman, D. E. Kingsmill, P. O. G. Persson, A. B. White, E. T. Strem, E. D. Andrews, and R. C. Antweiler, 2003: The impact of a prominent rain shadow on flooding in California's Santa Cruz Mountains: A CALJET case study and sensitivity to the ENSO cycle. *J. Hydrometeorol.*, **4**, 1243–1264.
- , —, and G. A. Wick, 2004: Satellite and CALJET aircraft observations of atmospheric rivers over the eastern North Pacific Ocean during the winter of 1997/98. *Mon. Wea. Rev.*, **132**, 1721–1745.
- , —, and R. Rotunno, 2005: Dropsonde observations in low-level jets over the northeastern Pacific Ocean from CALJET-1998 and PACJET-2001: Mean vertical-profile and atmospheric-river characteristics. *Mon. Wea. Rev.*, **133**, 889–910.
- , —, G. A. Wick, S. I. Gutman, M. D. Dettinger, D. R. Cayan, and A. B. White, 2006: Flooding on California's Russian River: The role of atmospheric rivers. *Geophys. Res. Lett.*, **33**, L13801, doi:10.1029/2006GL026689.
- , —, G. N. Kiladis, K. Weickmann, and D. M. Reynolds, 2011: A multi-scale observational case study of a Pacific atmospheric river exhibiting tropical-extratropical connections and a mesoscale frontal wave. *Mon. Wea. Rev.*, **139**, 1169–1189.
- Reeves, H. D., Y.-L. Lin, and R. Rotunno, 2008: Dynamic forcing and mesoscale variability of heavy precipitation events over the Sierra Nevada Mountains. *Mon. Wea. Rev.*, **136**, 62–77.
- Rutz, J. J., and W. J. Steenburgh, 2012: Quantifying the role of atmospheric rivers in the interior western United States. *Atmos. Sci. Lett.*, **13**, 257–261.
- Saha, S., and Coauthors, 2010: The NCEP Climate Forecast System reanalysis. *Bull. Amer. Meteor. Soc.*, **91**, 1015–1057.
- Shafer, J. C., W. J. Steenburgh, J. A. W. Cox, and J. P. Monteverdi, 2006: Terrain influences on synoptic storm structure and mesoscale precipitation distribution during IPEX IOP3. *Mon. Wea. Rev.*, **134**, 478–497.
- Smith, B. L., S. E. Yuter, P. J. Neiman, and D. E. Kingsmill, 2010: Water vapor fluxes and orographic precipitation over northern California associated with a land-falling atmospheric river. *Mon. Wea. Rev.*, **138**, 74–100.
- Steenburgh, W. J., and T. R. Blazek, 2001: Topographic distortion of a cold front over the Snake River plain and central Idaho mountains. *Wea. Forecasting*, **16**, 301–314.
- , C. R. Neuman, G. L. West, and L. F. Bosart, 2009: Discrete frontal propagation over the Sierra–Cascade mountains and intermountain west. *Mon. Wea. Rev.*, **137**, 2000–2020.
- Stewart, R. E., J. D. Marwitz, J. C. Pace, and R. E. Carbone, 1984: Characteristics through the melting layer of stratiform clouds. *J. Atmos. Sci.*, **41**, 3227–3237.
- Stohl, A., C. Forster, and H. Sodemann, 2008: Remote sources of water vapor forming precipitation on the Norwegian west coast at 60°N—A tale of hurricanes and an atmospheric river. *J. Geophys. Res.*, **113**, D05102, doi:10.1029/2007JD009006.
- Stonestrom, D. A., J. Constantz, T. P. A. Ferré, and S. A. Leake, Eds., 2007: Ground-water recharge in the arid and semiarid southwestern United States. U.S. Geological Survey Professional Paper 1703, 414 pp. [Available online at <http://pubs.usgs.gov/pp/pp1703/>.]
- Trabant, D. C., and G. P. Clagett, 1990: Measurement and evaluation of snowpacks. *Cold Regions Hydrology and Hydraulics*, W. L. Ryan and R. D. Crissman, Eds., American Society of Civil Engineers, 39–93.
- Viale, M., and M. N. Nuñez, 2011: Climatology of winter orographic precipitation over the subtropical central Andes and associated synoptic and regional characteristics. *J. Hydrometeorol.*, **12**, 481–507.
- Weber, B. L., D. B. Wuertz, D. C. Welsh, and R. McPeck, 1993: Quality controls for profiler measurements of winds and RASS temperatures. *J. Atmos. Oceanic Technol.*, **10**, 452–464.
- Wentz, F. J., 1995: The intercomparison of 53 SSM/I water vapor algorithms. Tech. Rep. on WetNet Water Vapor Intercomparison Project (VIP), Remote Sensing Systems, Santa Rosa, CA, 19 pp.
- West, G. L., and W. J. Steenburgh, 2010: Life cycle and mesoscale frontal structure of an intermountain cyclone. *Mon. Wea. Rev.*, **138**, 2528–2545.
- , and —, 2011: Influences of the Sierra Nevada on intermountain cold-front evolution. *Mon. Wea. Rev.*, **139**, 3184–3207.
- White, A. B., D. J. Gottas, E. Strem, F. M. Ralph, and P. J. Neiman, 2002: An automated bright-band height detection algorithm for use with Doppler radar vertical spectral moments. *J. Oceanic Atmos. Technol.*, **19**, 687–697.
- , F. M. Ralph, J. R. Jordan, C. W. King, D. J. Gottas, P. J. Neiman, L. Bianco, and D. E. White, 2007: Expanding the NOAA profiler network: Technology evaluation and new applications for the coastal environment. Preprints, *Seventh Conf. on Coastal Atmospheric and Oceanic Prediction and Processes*, San Diego, CA, Amer. Meteor. Soc., 8.6. [Available online at <https://ams.confex.com/ams/pdfpapers/127228.pdf>.]
- , and Coauthors, 2012: NOAA's rapid response to the Howard A. Hanson dam flood risk management crisis. *Bull. Amer. Meteor. Soc.*, **93**, 189–207.
- Wolter, K., and M. S. Timlin, 1998: Measuring the strength of ENSO events: How does 1997/98 rank? *Weather*, **53**, 315–324.
- Yin, H., 2005: A consistent poleward shift of the storm tracks in simulations of 21st century climate. *Geophys. Res. Lett.*, **32**, L18701, doi:10.1029/2005GL023684.
- Zhu, Y., and R. E. Newell, 1998: A proposed algorithm for moisture fluxes from atmospheric rivers. *Mon. Wea. Rev.*, **126**, 725–735.